TECHNISCHE UNIVERSITÄT DRESDEN

MAX-PLANCK-GESELLSCHAFT

mpipks

School of Science

Max-Planck-Institut für Physik komplexer Systeme

Attoclock Induced Electron Dynamics

Soumi Dutta

DISSERTATION

zur Erlangung des akademischen Grades

Doctor rerum naturalium (Dr. rer. nat.)

Eingereicht am 27.04.2021, Verteidigt am 11.10.2021

Eingereicht am

1. Gutachter:

2. Gutachter:

Abstract

Theoretical and experimental studies on intense laser atom interaction have drawn many interests over the past few decades. In this thesis, we consider strong-field tunnel ionization to explore two different problems dealing with the ionized-electron dynamics in the presence of an infrared, high-intensity, elliptically-polarized laser pulse. In the first part, we discover the electron dynamics from a static potential, this describes the complicated field-driven dynamics by a simple time-independent problem. In the second part, we set up an analytical expression for the attoclock offset angle. We use the time-dependent Kramers-Henneberger (KH) potential, and show how some approximations within the KH potential lead to the static potential and the analytical offset angle. We elucidate good agreement of our theory with the numerical results obtained from classical equations of motion. Finally, the comparison with the available experimental data has led to an interestingly new tunnel exit-radius different from the conventional models.

Contents

Abbreviations

SFA	strong field approximation
KH	Kramers-Henneberger
ADK	Ammosov, Delone and Krainov
CTMC	Classical-trajectory Monte Carlo
CW	continuous wave
FWHM	full width at half maximum
PMD	photo-electron momentum distribution
COLTRIMS	cold target recoil ion momentum spectroscopy
REMI	resonance microscope
SAE	single active electron
SMM	Simple-man's model
GSD	ground state depletion
OBI	over barrier ionization
CP	circularly polarized

RLV	Runge-Lenz vector
FDM	field direction model
KR	Keldysh-Rutherford
CCSFA	coulomb corrected strong field approximation
AKP	accelerated Kepler problem

Chapter 1

Introduction

In the year 2018, Gerald Mourau and Donna Strickland shared the Nobel prize in physics "for their method of generating high-intensity, ultra-short optical pulses" [1]. In recent years, availability of this ultra-short and high-intensity laser pulses has opened up an opportunity to measure the time duration of ultrafast processes in microscopic systems with a time-resolution of attosecond order $\sim 10^{-18}$ seconds [2]. This short time-interval can be clocked by means of the so called *pump-probe experiment* — a pump pulse starts the clock by triggering the microscopic motion; followed by a time delay, a probe pulse stops the clock when the process is captured. However, due to the high intensity, it is challenging to create two attosecond pulses for pump-probe spectroscopy. One way to avoid this attosecond double-pulses is the *attosecond streaking* [3] process.

In the *attosecond streaking* process, an extreme ultraviolet (XUV) attosecond laser pulse is used as a pump which ionizes a target atomic gas. The ionized electrons, after a time lapse, are streaked by using a femtosecond infrared (IR) laser pulse which acts as a probe [4, 5]. Here, the high energy XUV pulse is created from the low energy IR pulse by means of high-harmonic-generations (HHG). As a consequence, both pump and probe pulses are locked to each other. The streaking laser field changes the momentum of the ionized electrons by the vector-potential associated with it. The electron's final momentum/energy distribution as a function of pump-probe delay is used to extract various time-interval information such as, the attosecond pulse-duration [4], and also the time-delay of emitting an electron from an atom [2, 6].

Attosecond resolution can alternatively be achieved by the *angular-streaking* [7, 8], also known as *attoclock*. Unlike the *streaking* method, the attosecond pump pulse is not required here, instead a few-cycle nearly circularly-polarized IR pulse acts as a pump to create a non-linear tunnelling burst of electrons. On the other hand, the same pulse is used as the probe. In the presence of such low-frequency IR pulse, the atomic potential barrier does not oscillate fast, and in this quasi-static situation the bound electron can tunnel through the barrier — known as strong-field tunnel-ionization [9]. Due to the near-circular polarization of the applied field, electrons are emitted in different angular spatial directions, however, preferentially along the major axis of the pulse since the ionization probability is highest at the field-maximum. The distribution of final momenta of these electrons is measured at the detector which is in the pulse's polarization plane. It has a near-circular shape. Since the final momenta depend explicitly on the vector potential at the time of ionization, the angle of the measured momentum is usually mapped to the ionization time. Thus, the momentum vector plays the role of a clock-hand which performs a complete rotation over the clock-shaped detector in one optical cycle of the IR pulse ($\sim$ 3 fs for a wavelength of 800 nm), thereby, one-degree in the clock corresponds to ten attoseconds resolution.

After the tunnel ionization, far from the parent atom, the influence of the atomic potential is usually neglected which is known as strong-field approximation (SFA) [10–13]. Within this assumption, the final momentum of an electron is aligned along the vector potential at the ionization time. However, in reality, due to the long-range nature of the Coulomb potential, its effect on the electron dynamics might be relevant [14–20], e. g., in the attoclock setup, the final momentum vector makes an additional angel with respect to its direction predicted from strong-field approximation [7, 8]. This additional angle, corresponding to the most-probable electron at the field maximum, is sometimes called *attoclock offset angle* [21–23]. In addition to the Coulomb effect, a finite tunnelling time-delay — the time-lapse of an electron while tunnelling through the classically forbidden atomic potential barrier — is believed to have an impact on this offset angle [23, 24]. However, the existence of a finite tunnelling time is highly controversial [25–29], since it is inconsistent with the instantaneous quantum tunnelling [30].

In this thesis, we study the dynamics of the electrons after tunneling for which we do

not need to consider the debated tunnelling-time issue. Instead, we focus on the effect of Coulomb interaction on the ionized electron's dynamics. To analyse this effect, various theoretical models have been proposed, among them the Coulomb corrected strong field approximation (CCSFA) is one approach. This is a perturbative theory, where the final momentum is obtained by adding an impulse from the Coulomb potential to the SFA momentum, calculated with the SFA trajectory [15]. Adopting a similar perturbative approach, our goal is to find an analytical expression for the attoclock offset angle and to analyse the underlying effect of the Coulomb potential.

The laser-atom interaction Hamiltonian which governs the emitted electron's dynamics including the effect of Coulomb potential, can be described exactly by the length or velocity gauges. Alternatively, this laser-Coulomb interaction can be studied exactly in the Kramers-Henneberger (KH) frame [31, 32]. In this framework, the reference frame is fixed to the electron, therefore, the potential itself oscillates back and forth in the same way as the electron would oscillate in the laboratory frame. Generally, this fast oscillatory movement of the potential is averaged over one optical cycle, which results in a time-averaged *static potential* [33, 34]. A recent article in 2018 has shown that the time-averaged KH potential can be reduced to a pure Coulomb potential, and the electron dynamics driven by an elliptically-polarized pulse can be reproduced by this effective potential [35, 36]. Another work in the same year has revealed that a Rutherford scattering problem could predict the attoclock offset angle [37]. However, both theories are valid for low-intensity fields only, and in this thesis, we aim at constructing a static potential, so that the field-driven electron dynamics can be simply described by a time-independent problem in the strong field regime.

The thesis is organized as follows.

In chapter 2, the theoretical background of strong-field ionization is introduced necessary to understand the results in the following chapters. Chapter 3 focuses on the post-tunnelling ionization dynamics in the Kramers-Henneberger (KH) frame. We propose a static potential which simplifies the dynamics in the presence of an elliptically-polarized laser pulse. This static potential has an unconventional form, namely it has a ring-shaped singularity. In chapter 4, we will analyse the attoclock problem. It will be shown how using some new approximations motivated by the KH potential into the

Coulomb corrected strong field approximated method gives rise to an analytical attoclock angle, which agrees with the classical-trajectory Monte Carlo simulation (CTMC) [38–40] results. The tunnel exit points determine the initial conditions for the classical propagation, and have a sensitive impact on the final momentum vector. These exit points can not be directly measured in the experiment but can be modelled by different theoretical assumptions [21, 41, 42] which are, however, not unique. Therefore, it is important to obtain a realistic exit point. This is done in a new way by extracting the exit point via the analytical attoclock angle from experimental data. Finally, in chapter 5, the main results are summarized and an outlook is given.

Chapter 2

Intense laser-atom interaction

2.1 Introduction to strong-field physics

Interaction of atoms and molecules with the high-intense laser pulses leads to interesting multiphoton processes, where the energy of the incident laser pulse is so large that the target atoms or molecules absorb more than one photon. This may cause several interesting non-linear optical phenomena such as multiphoton excitation or ionization processes.

Strong-field ionization [9] is one of the distinct fundamental processes in strong-field physics, where the electrons in the atomic bound-state are ionized into the energy continuum triggered by the high-intense laser pulse. The intensities are so large that the force exerted by the laser pulse becomes comparable with the Coulomb force within the atomic systems, encoding information of microscopic processes. Typically, strong-field ionization processes occur at intensities of the order of atomic units (see appendix A for the details of atomic units).

Various ground-breaking physical phenomena have been discovered in the past years in this branch of physics. Namely, high harmonic generations (HHG) [43], above-threshold ionization (ATI) [44], frustrated tunnelling ionization (FTI) [16], and many other fascinating processes like coulomb focusing [14, 45, 46], formation of the low-energy structure (LES) [47–50], the zero-energy structure (ZES) [51–53], etc.

The interest of the thesis lies in the post-ionization dynamics of the electrons in the strong-field tunnelling-ionization process with a focus on the 'attoclock' experimental setup [7, 8, 21, 22]. Here in this chapter, all the required theoretical backgrounds are presented.

2.2 Definition of the laser pulses

A laser field is an electromagnetic wave which is radiated during stimulated emission of photons due to transition between different energy levels of an atom. The corresponding electric field which is of interest here, therefore, satisfies the Maxwell's equation,

$$\nabla^2 \vec{F}(\vec{r},t) - \frac{1}{c^2}\frac{\partial^2 \vec{F}(\vec{r},t)}{\partial t^2} = 0. \tag{2.1}$$

A plane-wave solution for $\vec{F}(\vec{r},t)$ satisfying Eq.(2.1), is given by,

$$\vec{F}(\vec{r},t) = \vec{F}_{\max}\cos(\vec{k}\cdot\vec{r} - \omega t). \tag{2.2}$$

This is a continuous wave (CW) laser field with $F_{\max}$, $\vec{k}$ and ω being the maximum field-strength, propagation vector and the central frequency of the laser, respectively. The corresponding peak intensity of the laser pulse is calculated as $I = |\vec{F}_{\max}|^2$.

Within the dipole approximation (see Sec. 2.3.2 for details), one can consider the electric field to be homogeneous. This translates to dropping the space dependence which yields the following simple form of the electric field,

$$\vec{F}(t) = \vec{F}_{\max}\cos(\omega t). \tag{2.3}$$

Generalizing the above equation for an elliptically-polarized laser in the xy plane, the corresponding electric field can be written as,

$$\vec{F}(t) = -F_\varepsilon(\varepsilon\sin(\omega t)\vec{e}_x + \cos(\omega t)\vec{e}_y), \tag{2.4}$$

with $F_\varepsilon = \dfrac{F_{\max}}{\sqrt{1+\varepsilon^2}}$. ε is the ellipticity of the field which lies between 0 (linear-polarization) and 1 (circular-polarization). Here, the choice of the ellipticity-dependent prefactor F_ε makes the average field intensity, $<I(t)> = <|\vec{F}(t)|^2>$, independent of ε.

A laser pulse is obtained as a superposition of plane waves using the principle of mode-locking [54, 55] with controllable peak-intensity and pulse-duration. To fulfil the conservation of energy and not to burn the systems, the larger peak-intensity can be procured with a shorter duration [56, 57]. This is achieved by increasing the number of consisting plane-waves required to be superimposed. Now, the finite duration of the pulse can be incorporated by using a suitable envelope function $f(t)$ into the electric field, resulting in

$$\vec{F}(t) = -F_\varepsilon\ f(t)(\varepsilon \sin(\omega t)\vec{e}_x + \cos(\omega t)\vec{e}_y). \tag{2.5}$$

Alternatively, we have defined the electric field through the vector potential $\vec{A}(t)$ as

$$\vec{F}(t) = -\frac{\partial \vec{A}(t)}{\partial t}, \tag{2.6}$$

where

$$\vec{A}(t) = \frac{-F_\varepsilon\ f(t)}{\omega}(\varepsilon \cos(\omega t)\vec{e}_x - \sin(\omega t)\vec{e}_y), \tag{2.7}$$

The electric field must satisfy

$$\int_{-\infty}^{\infty} dt \vec{F}(t) = 0. \tag{2.8}$$

In this thesis, we will consider the following two types of the envelopes

Gaussian :

$$f(t) = \exp\left(-\frac{\omega^2 t^2}{4N^2\pi^2}\right), \tag{2.9}$$

*Cos*4 :

$$f(t) = \begin{cases} \cos^4\left(\frac{\omega t}{2N}\right) & \text{if } |t| \leq \frac{N\pi}{\omega} \\ 0 & \text{otherwise,} \end{cases} \tag{2.10}$$

where N is the number of optical cycles within the pulse.

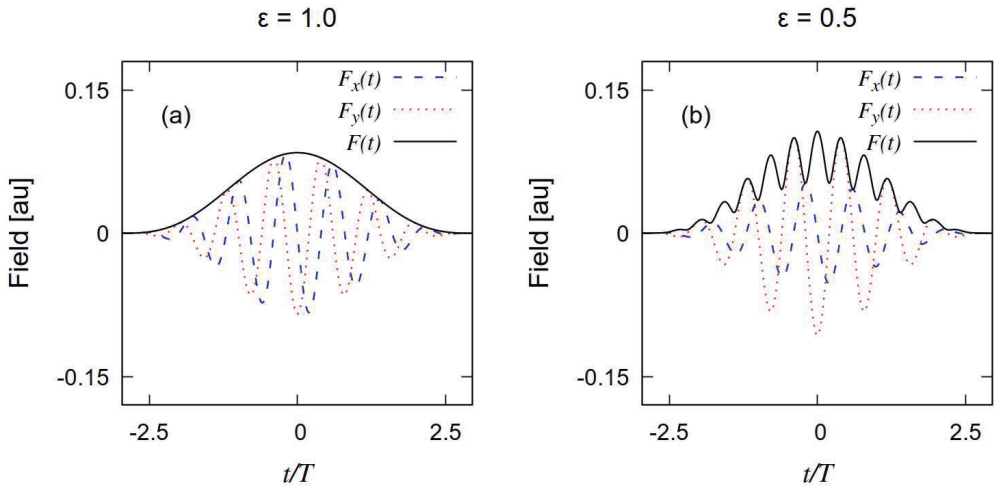

FIGURE 2.1: The electric field $\vec{F}(t)$ from Eq. (2.6) (with the vector potential $\vec{A}(t)$ from Eq. (2.7)) as a function of time t in units of laser period T. The x and y component of $\vec{F}(t)$ i. e. $F_x(t)$ and $F_y(t)$, and the field-amplitude $F(t) = |\vec{F}(t)| = \sqrt{F_x(t)^2 + F_y(t)^2}$ are shown for two ellipticities (a) $\varepsilon = 1.0$ (circular-polarization) and (b) $\varepsilon = 0.5$. Here, the pulse envelope $f(t)$ is used as the Cos4 envelope, cf. Eq. (2.10) with number of optical cycles $N = 6$. Here, frequency $\omega = 0.058$ au (which corresponds to a wavelength $\lambda = 800$ nm), and the intensity $I = 5 \times 10^{14}$ Wcm^{-2}.

A typical picture of the electric field as defined by Eq. (2.6) with $\vec{A}(t)$ from Eq. (2.7) are shown for two ellipticities in Fig. 2.1.

2.3 Approximation schemes

To understand the fundamentals of intense laser-atom interaction a number of approximation schemes have been developed along with necessary transformation rules. This section is devoted for the discussion on those approximations which will be regularly used in later chapters.

2.3.1 Single-active-electron approximation

The single-active-electron (SAE) approximation is one of the popularly used approximation in strong-field physics. SAE considers that only one electron in the outer-most orbit

of the atom is active for ionization. Later we see that the probability of strong-field ionization is an exponentially decreasing function of the ionization potential I_p, cf. Eq. (4.9). Therefore SAE becomes a valid approximation as the probability of ionizing the inner electrons becomes negligible.

The minimal-coupling interaction Hamiltonian (also known as velocity gauge) within such SAE approximation is given by

$$H(\vec{r},\vec{p},t) = \frac{(\vec{p}-\vec{A}(\vec{r},t))^2}{2} + V(\vec{r}), \tag{2.11}$$

with $V(\vec{r}) = -\dfrac{1}{|\vec{r}|}$ is the potential energy representing Coulomb interaction between the single-active electron and the singly-charged parent ion. Atomic units (appendix A) have been used here. The vector potential $\vec{A}(\vec{r},t)$ can be obtained within the dipole approximation as described below.

2.3.2 Dipole approximation

The dipole approximation consists in neglecting the atomic dimension $\vec{r}$ in the vector potential $\vec{A}(\vec{r},t)$, i. e.

$$\vec{A}(\vec{r},t) = \vec{A}(0,t). \tag{2.12}$$

This approximation is valid when $\vec{k}\cdot\vec{r} \ll 1$, which is readily satisfied because the atomic dimension $\vec{r}$ (of the order of angstrom) is much smaller than the wavelength λ (of the order of several hundreds of nanometer) of the laser pulse. Within such approximation, the vector potential $\vec{A}(t)$ for an elliptically-polarized laser pulse can be given by Eq. (2.7).

At this point, one should note that the Lorentz force originating from the magnetic field $\vec{B}$ can be neglected within the dipole approximation because $\vec{B} = \vec{\nabla}\times\vec{A}(t) = 0$. This also means that the relativistic effect can be neglected, in other words, the velocity of the electron v is much smaller than the speed of light c. For the intensities I and wavelength λ used in this thesis (I lies between 10^{13} and 10^{15} Wcm^{-2}, and λ lies between 400 and 800 nm), $v \ll c$ is fulfilled [58, 59]. Hence the relativistic effect can be neglected safely.

2.3.3 Length gauge interaction

Let us now describe, within the dipole approximation, the following Gauge transformation [60] used in classical electromagnetic theory with the scalar and the vector potential ϕ, and $\vec{A}$, respectively

$$\phi' = \phi - \frac{\partial \chi}{\partial t}, \tag{2.13a}$$

$$\vec{A}' = \vec{A} + \nabla\chi. \tag{2.13b}$$

Using the above transformation with the scalar field

$$\chi(\vec{r}, t) = -\vec{r} \cdot \vec{A}(t), \tag{2.14}$$

the minimal coupling Hamiltonian in Eq. (2.11) is reduced to

$$H_l(\vec{r}, \vec{p}, t) = \frac{\vec{p}^2}{2} + \mathrm{V}(\vec{r}) + \vec{r} \cdot \vec{F}(t). \tag{2.15}$$

Here, $\vec{r} \cdot \vec{F}(t)$ represents the interaction energy between the E-field and the field-induced dipole moment created between the ionized electron and the parent ion. Coulomb gauge ($\phi = 0$) is used here [61].

Because the electric field is coupled with the position vector, such an interaction picture is known as length-gauge. This picture provides us an understanding of the strong-field tunnelling-ionization process in the presence of a low-frequency and intense laser pulse, which is schematically shown in Fig. 2.2, and discussed in the next section.

2.4 Strong-field ionization - overview and classification

When the external laser field is strong enough, instead of being excited from energetically lower to higher bound-state, the electron, enters the continuum, and ionized from the atomic system. Depending on the pulse parameters and the atomic potential, the strong-field ionization processes can be described by different scenarios. There are mainly two

different ionization channels, which are — the tunnelling ionization and the multiphoton ionization [62, 63].

The above mentioned two regimes can be differentiated by a distinguishing parameter γ as introduced by Keldysh [10] — known as Keldysh parameter — which depends on the intensity I, frequency ω of the laser pulse, and the ionization potential I_p of the atom. The definition reads,

$$\gamma = \sqrt{\frac{I_\mathrm{p}}{2U_\mathrm{p}}}, \tag{2.16}$$

where $U_\mathrm{p} = I/4\omega^2$ is the cycle-averaged kinetic energy of a free electron in the presence of a quivering laser field. U_p is known as the ponderomotive energy.

γ can be interpreted as the barrier traversal phase i. e. the phase corresponding to the tunnelling time. Now, for an electron to tunnel before the electric field has turned around, $\gamma \ll 2\pi$ should be satisfied. Therefore, to be on the safe side, if $\gamma \ll 1$ is fulfilled, which is valid for low frequencies, the tunnelling ionization is the dominant process in this limit. Whereas, in the opposite limit, for high frequencies i. e. for $\gamma \gg 1$, multiphoton ionization — ionization by absorbing multiple photons, is the dominant process. The interest of this thesis rests on — *tunnelling ionization*, which is discussed below.

2.4.1 Tunnelling ionization

For a low-frequency laser pulse, the characteristic time of an electron in the atomic bound-state is much smaller than the pulse period. For example, the time required for an electron to orbit around the nucleus in a hydrogen atom is about 150 attoseconds (1 as $= 10^{-18}$ s) [64], whereas, for an infrared pulse with a typical wavelength of 800 nm, the pulse period is 2600 as ($\gg$ 150 as). In this low-frequency limit, time can be treated as a parameter, and the electron can tunnel through a time-independent potential barrier (Fig. 2.2) formed by the instantaneous laser field and the atomic Coulomb potential. This quasi-static (adiabatic) ionization process is known as the tunnelling ionization. The above scenario is depicted in Fig. 2.2.

The effective potential is modulated as a function of time due to the oscillation of the pulse. In the presence of a linearly-polarized pulse, cf. Eq. (2.3), the effective potential

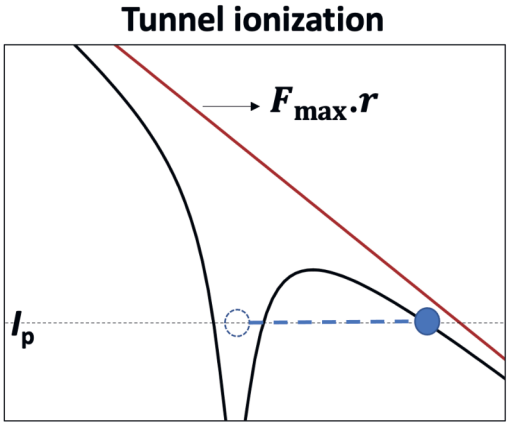

FIGURE 2.2: The strong-field tunnelling ionization. The effective Coulomb potential $V(\vec{r},t)$, cf. Eq. (2.17), is bent down (black solid curve) within the length-gauge (Eq. (2.15)) interaction between the atom and the instantaneous field-maximum (which corresponds to $t = 0$, here), as given by $\vec{F}_{\rm max} \cdot \vec{r}$ (brown solid line). This interaction makes the barrier width low enough and therefore the bounded electron (blue dotted circle), which is sitting at the ionization potential $I_{\rm p}$ (black dotted line) of the atom, can tunnel through the barrier (blue dashed path). The electron comes out of the potential at the tunnel-exit located at $r = r_e$ (blue solid circle).

from Eq. (2.15) can be written as

$$V(\vec{r},t) = V(\vec{r}) + \vec{r} \cdot \vec{F}_{\rm max} \cos(\omega t). \tag{2.17}$$

At an instant $t = 0$, this effective potential has been shown in Fig. 2.2. We can see that the Coulomb potential $V(\vec{r})$ bends down in the presence of the interaction term $\vec{r} \cdot \vec{F}_{\rm max}$, making the barrier-width lower especially with higher $F_{\rm max}$. The electron can easily tunnel through this low barrier. If the field-strength is too high, the barrier is suppressed so much that the electron is released over the top of the barrier, which is known as 'over barrier ionization (OBI)' [65].

Now, the dynamics of tunnelling is classically forbidden which requires to incorporate quantum effect, and therefore, this is beyond the scope of simple Newtonian mechanics. However, we are interested to study and explore the classical electron dynamics after it has tunnelled out. Therefore it is crucial to know the initial coordinates of the electron at the end of such a tunnelling process. Although the initial position and momentum can not be measured directly in an experiment, different theoretical models can predict them depending on different tunnelling geometry. We will discuss about those related to initial

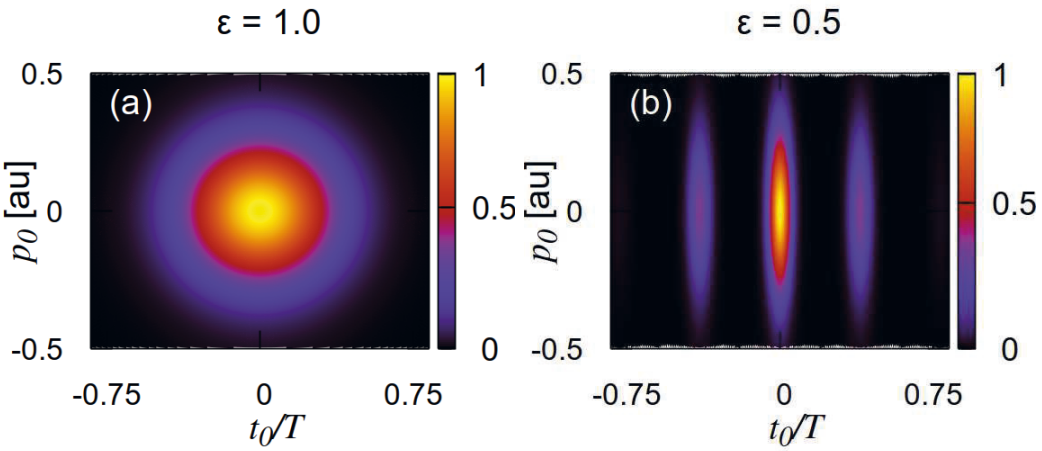

FIGURE 2.3: Total probability distribution function corresponding to the tunnelling ionization within the ADK model, cf. Eq. (2.20), as a function of the initial time t_0, and the initial momentum p_0, for the laser pulse in Fig. 2.1. It can be noticed that the distribution follows the field amplitude $F(t) = \sqrt{F_x(t)^2 + F_y(t)^2}$, which is shown by the black solid-line in Fig. 2.1, for the two different ellipticities of this figure in (a) and (b). Since the distribution function falls exponentially with the field-amplitude $F(t_0)$, the relevant ionization events are occurring only near the maxima of the field, and the distribution is Gaussian in p_0, cf. Eq. (2.18).

position later in appendix E. The probability of the initial momentum follows a Gaussian distribution, peaked around zero-momentum in the quasi-static situation, which is given by

$$R_1(\vec{p}_0, t_0) = \frac{(2I_\mathrm{p})^{1/4}}{\sqrt{\pi F(t_0)}} \exp\left(- \frac{\sqrt{(2I_\mathrm{p})}\vec{p}_0^{\,2}}{F(t_0)} \right) \tag{2.18}$$

where $F(t) = |\vec{F}(t)|$ is the instantaneous field amplitude of the electric field. t_0 and $\vec{p}_0$ are the initial time and momentum, respectively. One should also incorporate the tunnelling-ionization rate in determining the initial conditions. For a 3D Hydrogen atom with $F(t_0) \ll 1$, it is given by [66]

$$\Gamma(F(t_0)) = \frac{4}{F(t_0)} \exp\Big[- \frac{2}{3F(t_0)} \Big]. \tag{2.19}$$

Ammosov, Delone, and Kranov (ADK) [10, 67, 68] have generalized the above relation for any atom, and incorporating this rate, initially the electron trajectory can be weighted by

$$R_{\mathrm{ADK}}(\vec{p}_0, t_0) = C_l^2 \frac{2l+1}{2} \left(\frac{4I_\mathrm{p}}{F(t_0)} \right)^{\frac{2}{\sqrt{2I_\mathrm{p}}}-1} \exp\left(\frac{-2(2I_\mathrm{p})^{3/2}}{3F(t_0)} \right) R_1(\vec{p}_0, t_0). \tag{2.20}$$

l is the angular-momentum quantum number of the initial bound state of atom. The values of l and the normalization constant C_l are taken from Ref. [69]. The ADK distribution of initial coordinates (p_0, and t_0) is depicted in Fig. 2.3 for the laser in Fig. 2.1.

It is important to note that the ADK theory is justified far into the tunnelling regime, i. e. the potential barrier does not move during the ionization process. On the contrary, when the frequency is higher, the adiabatic scenario does not valid any more. One has to consider the time-dependent motion of the potential (Eq. (2.17)), and then the system can just be described by the superposition of several adiabatic states. The electrons gain energy from such a time-dependent potential barrier, and as a result the effective barrier becomes thinner. This is known as non-adiabatic tunnelling ionization [70, 71]. The γ value in the non-adiabatic regime, lies between the multiphoton and the tunnelling regime i. e. $\gamma \approx 1$ (See Perelomov, Popov, Terent'ev (PPT) model [72, 73]).

2.5 Electron trajectory in strong-field physics

Within strong-field approximation, after tunnelling out from the atom, the electron moves almost freely in the presence of an oscillatory laser field. Depending on its initial coordinates at the tunnel exit, the almost-free electron — either scatter back with the parent ion, or can fly off forever — exhibit many interesting phenomena in strong-field physics. For example, re-scattering with the parent ion with a very high-energy exchange can cause high-energy-photon production known as high-harmonic generation (HHG). Whereas, re-scattering with low energies, which is known as soft re-scattering, has nice applications like capturing into the atomic excited state with high quantum-number — a phenomena called Rydberg state formation, also known as frustrated tunnelling ionization (FTI). Such soft re-scattering can also explain the mechanism of forming the well-known low-energy structure (LES) [47], very low-energy structure (VLES), zero-energy structure (ZES) [51–53] in the photo-electron spectra.

However, on the other hand, the emitted electron can also reach the detector (which is asymptotically far away from the system) without any re-scattering, — these are naturally termed as direct electrons. The ionization of these direct electrons with a near circularly-polarized laser pulse are applied to study the 'attoclock' problem where the final angle of the momentum in the photo-electron momentum plane is usually mapped to the electron's released time. Remarkably, this allows to study interesting temporal behaviour of various microscopic processes within attosecond precision.

In the next section, we will analyse an electron's trajectory in the presence of a pure oscillatory laser pulse classically through the lens of a simple theory, commonly known as Simple-man's model (SMM) [74–76]. Surprisingly, SMM can explain the strong-field ionization and various re-collision process reasonably well, of course with certain but acceptable limitations.

2.5.1 Simple-man's model

Within strong-field approximation (SFA) [10–12], the electron's trajectory can be described by the Simple-man's model, where a zero-range potential is considered i.e. $V(r) = 0$ everywhere except at $r = 0$.

The initial coordinates at the release time t_0 are chosen to be

$$\vec{r}(t_0) = \dot{\vec{r}}(t_0) = 0. \tag{2.21}$$

For all time $t > t_0$, the electron trajectory is driven by the oscillatory laser and follows the Newton's equations of motion

$$\ddot{\vec{r}}(t) = \vec{F}(t). \tag{2.22}$$

This is obtained using atomic unit within the Lorentz-force $e\vec{F}(t)$, with the contribution due to magnetic-field $\vec{B}(t)$ being neglected within dipole-approximation. Equation (2.22), with the initial conditions given in Eq. (2.21), is integrated to result in the following

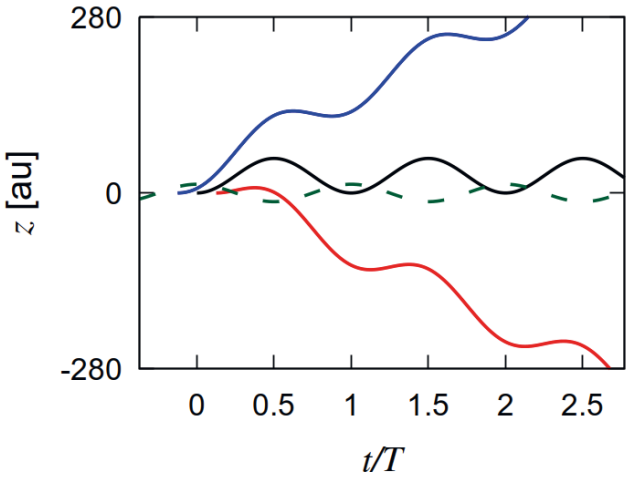

FIGURE 2.4: The Simple-man's trajectory, cf. Eq. (2.24b) for three values of the release time t_0: $t_0 = -T/8$ (blue curve), $t_0 = 0$ (black curve), and $t_0 = T/8$ (red curve). The dashed curve is the scaled electric field of Eq. (2.3), linearly-polarized along $\hat{z}$.

solutions for the electron's velocity $\dot{\vec{r}}(t)$, and the electron's trajectory $\vec{r}(t)$

$$\dot{\vec{r}}(t) = \vec{A}(t_0) - \vec{A}(t) \tag{2.23a}$$

$$\vec{r}(t) = \vec{A}(t_0)(t - t_0) - \int_{t_0}^{t} dt' \vec{A}(t'), \tag{2.23b}$$

For the co-sinusoidal pulse in Eq. (2.3), the above Eqs. (2.23) reduce to

$$\dot{\vec{r}}(t) = \frac{-\vec{F}_{\max}}{\omega}(\sin(\omega t_0) - \sin(\omega t)) \tag{2.24a}$$

$$\vec{r}(t) = \frac{-\vec{F}_{\max}}{\omega}\Big(\sin(\omega t_0)(t - t_0) + \frac{\cos(\omega t) - \cos(\omega t_0)}{\omega}\Big). \tag{2.24b}$$

The first term being constant and linear in time, respectively, for the velocity and the position, is known as the drift term, and the second term is the quiver term.

The above trajectories are plotted for different t_0 in Fig. 2.4 for a linearly-polarized laser pulse along the z axis. We can see that depending on different t_0, the asymptotic velocities of the released electrons are very different, which are obtained as the following

$$\dot{\vec{r}}(t \to \infty) = \vec{A}(t_0) - \vec{A}(t \to \infty), \tag{2.25}$$

The final velocity depends only on the initial coordinates at the released time t_0 for a

finite-duration pulse when $\vec{A}(t \to \infty)$ becomes 0. The electron trajectory released at the field-maximum ($t_0 = 0$, cf. Eq. (2.3)) obtain a zero drift momentum. However, the trajectories released a little before and after the field-maximum acquire a positive and negative drift momentum, respectively, as shown in Fig. 2.4.

If the electron comes back to the ion, which is assumed to be placed at $\vec{r} = 0$, after it has ionized, it can re-collide with the ion as discussed previously. Depending on the values of the momentum at return, different phenomena such as HHG, FTI, or the formation of the LES takes place. HHG occurs when the electron returns and recombines with high momentum. On the contrary, chances of FTI or the LES events become high when the momentum of the returning electron is comparatively low. The returning energy/momentum, calculated within the simple man's model, sometimes beautifully predicts the features of the corresponding spectrum [77].

However, in this thesis we are interested in the final momentum of the direct electrons, particularly applied to an attoclock setup, as will be introduced below, where the final momentum can not be given just by Eq. (2.25), rather it is shifted by an offset.

2.5.2 Attoclock offset

The attoclock [7], also known as attosecond-angular-streaking, is based on the principle of streaking-camera [78], where a light is incident on a rotating mirror and the photons arrived at different times get deflected to different positions measured at the detector. Hence, one can estimate the intensity of the incoming light as a function of time. Similarly, in the attoclock experiment, the tunnel-ionized electrons from atoms at different instances of the incident laser pulse, which is a low-frequency, intense, and near circularly-polarized (CP) pulse, get deflected to different asymptotic momentum measured at the detector. The angle of the asymptotic momentum in the momentum plane (basically the near-circular polarization-plane) is usually connected to the ionization time, and thus time is mapped to the dial of a near-circular clock, which has different applications, e. g., in estimating the photo-ionization delay time, photo-emission or photo-absorption time, etc. with attosecond accuracy. The CP pulse in the attoclock plays the role of a rotating mirror in the streaking camera.

Within SFA, the final momentum is perpendicular to the initial electric field (see Eq. (2.25)), however, in the real experiment, the final momentum makes an additional angle with this perpendicular direction. For the most-probable electron, this additional angle is referred to as the *attoclock offset angle*. This offset value originates from the laser-Coulomb interaction, which is ignored in the SFA. However, it is also sometimes inferred that a finite tunnelling-time contributes to this offset value, which has been studied in several recent experimental and theoretical works [23, 24, 79, 80]. The extraction of finite tunnelling-time is highly debated since tunnelling-time does not exist as such [22, 37, 41, 42, 81].

Therefore, the final momentum can be modified as the following

$$\dot{\vec{r}}(t \to \infty) = \vec{A}(t_0) + \vec{p}_{c,t_0}, \tag{2.26}$$

$\vec{p}_{c,t_0}$ is the shift in the final momentum due to the Coulomb interaction. The derivation of getting $\vec{p}_{c,t_0}$ is not straightforward, as the dynamics, in the combined effect of the laser pulse and the Coulomb attraction force from the parent ion, is complicated. Several theoretical approaches have been adapted to obtain the $\vec{p}_{c,t_0}$, thereby the corresponding attoclock offset angle [20, 82, 83]. The Coulomb corrected SFA calculations have been discussed in ref. [82], where the momentum shift is obtained as the impulse from the Coulomb potential using the SFA trajectory. This is a kind of perturbative approach. A similar approach with the Kramers-Henneberger (KH) potential has been used in ref. [20], where the momentum shift is obtained as an impulse from the KH potential using the KH-potential-free trajectory. We will be dealing with the latter approach [20] and discuss some approximation leading to an analytical expression for the offset angle. The approximations are based on dividing the whole intensity area of a typical experimental offset angle vs. intensity graph (see Fig. 2.5) into two zones — the low-intensity and high-intensity zones, which will be discussed in chapter 4 of this thesis.

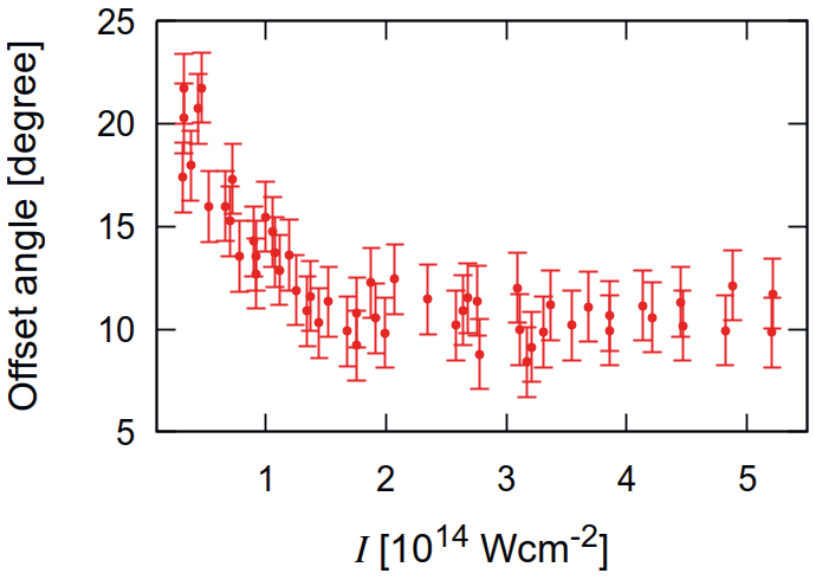

FIGURE 2.5: The offset angle as a function of intensity I in an attoclock experiment. The data of this figure is extracted from Boge *et al* [84].

2.6 Summary

The focus of this thesis is the analysis of the electron's trajectory applied to an attoclock setup. The prerequisite theory to understand the primary observable in the attoclock experiment is presented in this chapter. Attoclock typically deals with elliptically-polarized laser pulses. In the presence of such an elliptically-polarized pulse, the final momentum along the minor axis of the polarization ellipse can be obtained by a Simple-man's model [18]. However, for ellipticities $\varepsilon > 0.3$, the loss of Coulomb focusing effect [85] and the emergent of Coulomb asymmetry [18] lead to a deviation in the final momentum along the major axis of the polarization ellipse from the Simple-man's model. This deviation is also encountered in the polar angle of the final photoelectron momentum plane, thereby in the offset angle, which is defined as the inclination of the most-probable electron's actual momentum with respect to the SFA momentum. However, obtaining the deviation analytically, is difficult, since the dynamics has to be considered in the combined presence of the oscillatory laser pulse and the Coulomb interaction with the parent ion. The Coulomb corrected SFA (CCSFA) theory in this context was introduced by Goreslavski

et al [15], which has been later extended in refs. [18, 20].

In the next chapter, we will study the electron's field-driven dynamics from a static potential, where the field dependence only comes through the parameters within the potential and the initial conditions of the electrons. The chapter following the next will discuss different approximations within the CCSFA approach to obtain the above momentum deviation analytically.

Chapter 3

Strong-field trajectory from a static potential

3.1 Introduction

Interaction of atoms with intense low-frequency laser fields leads to tunnel ionization of an electron from an atom. We study the ionized electron's dynamics in the combined presence of the Coulomb potential and the external oscillatory laser field classically. The trajectories of the ionized electrons are complicated. In recent publications [35]-[36], this complicated dynamics has been reduced with a "guiding-center framework" simplifying the electron trajectory within an effective static potential description. However, this framework is limited to the laser pulses with low-intensity and shows a deviation in the interesting high-intensity regime.

This chapter focuses on formulating a static potential that can describe the tunnel-ionized electron's full dynamics driven by a laser field. To obtain this simplified description with a static potential, we use the Kramers-Henneberger (KH) Hamiltonian, in which the electron dynamics becomes easier to analyse, as discussed in section 3.2.

The exact time-dependent KH trajectory is dominated by the time-independent zeroth-order term in a series-expansion of the KH potential. Moreover, the total energy is almost

constant as a function of time for the KH trajectory (section 3.3). Both of these facts serve as a clue for the existence of a static potential.

We will show that the electron experiences the time-dependent KH potential for a short initial time after it gets ionized. Within this short time, it flies away very quickly from the parent ion. For a nearly circularly-polarized laser pulse, a short-time expansion of the KH potential leads to a static ring potential, which is discussed in section 3.4.1. Surprisingly, this static ring potential reproduces the ionized electron's field-driven trajectory very well for high-intensity and nearly circularly-polarized laser pulses.

Another simplified description for the tunnel-ionized electron dynamics can be achieved by setting up a rotated Kepler problem (section 3.4.2). The electron trajectory follows a Kepler hyperbola for low-intensity laser pulses. For high-intensities, the latter deviates from the real trajectory but can capture it when introducing a rotation.

3.2 Kramers-Henneberger frame

In the Kramers-Henneberger (KH) frame [31, 32], also known as the acceleration formulation of light-matter interaction, the potential becomes time-dependent and the corresponding laser-atom interaction problem is described by the following Hamiltonian

$$H_{\mathrm{kh}}(\vec{r},\vec{p},t) = \frac{\vec{p}^{\,2}}{2} + V(\vec{r}-\vec{r}_{\mathrm{q}}(t)), \tag{3.1}$$

where $V(\vec{r}) = -1/\mid \vec{r} \mid$ is the Coulomb potential. $\vec{r}_{\mathrm{q}}(t)$ is the quiver position co-ordinate and it is related to the acceleration $\ddot{\vec{r}}_{\mathrm{q}}(t) = \vec{F}(t)$ (see Eq. (2.22)) of the electron,

$$\vec{r}_{\mathrm{q}}(t) = \int_{t_0}^{t} dt'' \int_{t_0}^{t''} dt' \; \vec{F}(t'), \tag{3.2}$$

where $\vec{F}(t)$ is the electric field of an elliptically-polarized laser, calculated using Eq. (2.6) with the corresponding vector potential is taken from Eq. (2.7). The pulse envelope $f(t)$ is chosen as the following.

$$f(t) = 1, \text{ for a continuous wave (CW) laser.}$$
$$f(t \to \pm\infty) = 0, \text{ for a finite laser pulse.}$$

It is clear from Eq. (3.1) that in the KH potential, the Coulomb singularity moves with time t and is located at $\vec{r} = \vec{r}_{\rm q}(t)$. Now for a CW laser pulse, $\vec{r}_{\rm q}(t)$ is expressed as

$$\vec{r}_{\rm q,CW}(t) = r_{\rm q}\,(\cos(\omega t)\,\vec{e}_y + \varepsilon\,\sin(\omega t)\,\vec{e}_x), \tag{3.3}$$

where $r_{\rm q} = F_\varepsilon/\omega^2$ is the quiver amplitude. Therefore, the singularity $\vec{r}_{\rm q}(t)$ moves on an ellipse with ellipticity ε in the plane of polarization (xy plane). The motion of the singularity maximally extends to $r_{\rm q} = |\vec{r}_{\rm q,CW}(0)|$, which also defines the major axis of the polarization ellipse (as shown by a blue arrow in Fig. 3.1). Naturally, the quiver amplitude $r_{\rm q}$ increases with decreasing ellipticity, as can be seen also from Fig. 3.1.

Whereas in case of a finite laser pulse, $\vec{r}_{\rm q}(t)$ shrinks with time and ends up at the origin at the end of the pulse, on the contrary, for a CW pulse, it continues to move along the edge of the polarization ellipse. Figure 3.1 shows the movement of the KH potential for three different ellipticities.

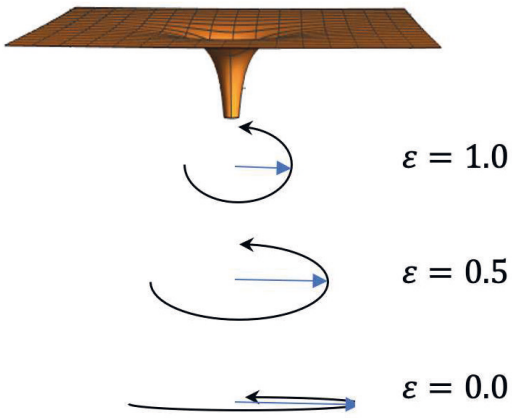

FIGURE 3.1: The motion of the Coulomb singularity in the KH frame, for a circularly-polarized (ellipticity $\varepsilon = 1.0$), an elliptically-polarized (ellipticity $\varepsilon = 0.5$), and a linearly-polarized (ellipticity $\varepsilon = 0$) laser pulse. The singularity of the KH potential lies at $r = \vec{r}_{\rm q}(t)$, therefore the blue arrow represents $\vec{r}_{\rm q}(t = 0)$, whose magnitude is given by $r_{\rm q} = \dfrac{F_\varepsilon}{\omega^2}$ (cf. Eq. (3.3)).

In the presence of a low-frequency and high-intensity laser pulse, the electron in the atomic bound state undergoes tunnel-ionization, which is discussed in chapter 2. In the subsequent sections, we will discuss the strong-field-driven trajectory in the KH frame after tunnelling out from the atom. We will see that the dynamics of the electrons become easier to analyse as compared to that in the length-gauge. Interestingly, such a framework allows us to obtain an effective static potential that governs the tunnel-ionized electron's real trajectory as we will discover later.

3.2.1 From quivering to no-quivering trajectory

Here we discuss the coordinate transformation which is necessary to go from laser-atom interaction in length gauge to the KH frame. For this purpose, let us examine the two interaction gauges, i. e. the length gauge and the velocity gauge. The length gauge formulation of light-matter interaction is defined by the following Hamiltonian

$$H_{\mathrm{l}}(\vec{r},\vec{p},t) = \frac{\vec{p}^{\,2}}{2} + \mathrm{V}(\vec{r}) + \vec{r}\cdot\vec{F}(t), \tag{3.4}$$

whereas the velocity gauge formulation, also known as minimally coupled interaction, is defined by

$$H_{\mathrm{v}}(\vec{r},\vec{p},t) = \frac{(\vec{p}-\vec{A}(t))^2}{2} + V(\vec{r}). \tag{3.5}$$

The electron dynamics in these two Hamiltonian in Eq. (3.4) and Eq. (3.5) are identical to each other, as the corresponding Lagrangian differs from each other by a total time derivative of a function. This results in the same equations of motion for both gauges.

The quiver momentum $\vec{p}_{\mathrm{q}}(t)$ is defined by

$$\vec{p}_{\mathrm{q}}(t) = \dot{\vec{r}}_{\mathrm{q}}(t) = \int_{t_0}^{t} dt\vec{F}(t) = -\vec{A}(t). \tag{3.6}$$

Using the $\vec{p}_{\mathrm{q}}(t)$ from Eq. (3.6) and the following coordinate transformation,

$$\vec{r}(t) = \vec{r}(t) + \vec{r}_{\mathrm{q}}(t) \qquad\qquad \vec{p}(t) = \vec{p}(t) + \vec{p}_{\mathrm{q}}(t), \tag{3.7}$$

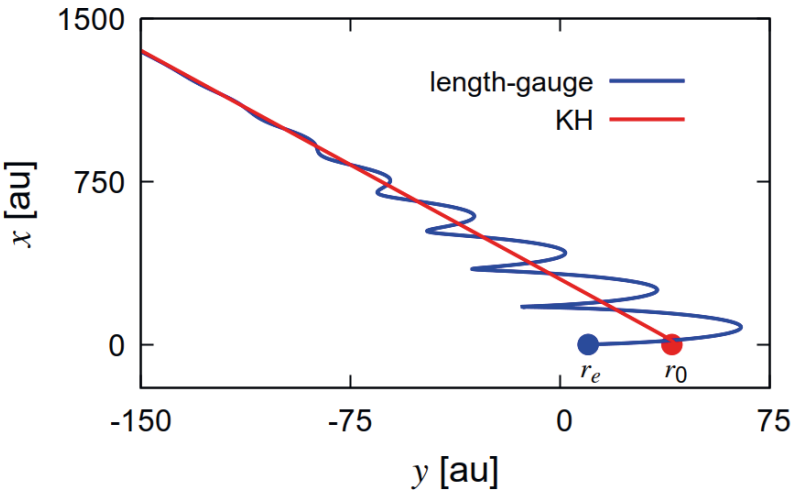

FIGURE 3.2: Electron trajectory in the plane of polarization. The blue trajectory is the one obtained by solving the equations of motion, numerically, in the length-gauge Hamiltonian H_l (Eq. (3.4)) with initial phase space coordinates (r_e, p_e) and the red trajectory is the corresponding trajectory in the KH interaction picture (Eq. (3.8)) with initial phase space coordinates (r_0, p_0) (cf. Eq. (3.9)). The corresponding initial points for these two interaction picture are shown by the circles. Laser parameters used at wavelength $\lambda = 800$ nm, ellipticity $\varepsilon = 0.8$, intensity $I = 8 \times 10^{14}$ W/cm^2. A Gaussian envelope function Eq. (2.9) has been used here, with $N = 5$ and an ionization potential $I_\mathrm{p} = 0.9$ au is used corresponding to helium.

the KH Hamiltonian is obtained as

$$H_\mathrm{kh}(\vec{r}, \vec{p}, t) = \frac{\vec{p}^{\,2}}{2} + V(\vec{r} - \vec{r}_\mathrm{q}(t)). \tag{3.8}$$

We solve Hamilton's equations of motion for the KH Hamiltonian with the following initial position and momentum

$$\vec{r}_0 = \vec{r}_e + \vec{r}_\mathrm{q}(t_0) \qquad\qquad \vec{p}_0 = \vec{p}_e + \vec{p}_\mathrm{q}(t_0). \tag{3.9}$$

$(\vec{r}_e, \vec{p}_e)$ are the phase-space coordinates defining the tunnel exit. r_e defines the barrier width, which can be calculated in the length-gauge using the energy conservation at the tunnel-exit. This is discussed in chapter 4 in section E. In this chapter, we use the field-direction model for r_e, taken from Eq. (E.2). The exit momentum p_e is assumed to be zero: at the tunnel-exit point the kinetic energy of the electron is zero since the total energy equals the potential energy [14, 77, 86].

Figure (3.2) shows two trajectories. One is the trajectory obtained by solving Hamilton's equations of motion for H_{l} with initial phase-space coordinates ($\vec{r}_e$, $\vec{p}_e$) (blue line), and the other is obtained from H_{kh} with initial phase-space coordinates ($\vec{r}_0$, $\vec{p}_0$) (red line). We see that for the electron trajectory in the KH frame, the wiggles from the time-dependent oscillatory field are not visible, as they show up for the length-gauge case. This already simplifies the dynamics in the KH Hamiltonian. However, this is still a time-dependent problem, whereas we search for a possible static potential governing the electron's dynamics in the remaining sections, using this easy description of motion within this KH frame.

Next, we analyse various terms in a series expansion of the KH potential. The zeroth-order terms of this series correspond to the cycle-averaged KH potential, and this is time-independent. The limits of describing the ionized electron's trajectory within such a time-independent description will be discussed.

3.2.2 Analysis of a series-expansion of the KH potential

The discussion is sometimes easier when one neglects the envelope. For sufficiently long pulse the envelope is approximately constant for the relevant part of the pulse. Therefore, $\vec{r}_{\mathrm{q}}(t)$ can be given by $\vec{r}_{\mathrm{q,CW}}(t)$, cf. Eq. (3.3). Whereas, for a finite laser, one can approximate that the envelope $f(t)$ changes slowly with time compared to the fast-oscillatory sinusoidal terms with frequency ω in Eq. (2.7). Within this approximation, we can take out $f(t)$ outside of the integration Eq. (3.2), resulting in the following expression for $\vec{r}_{\mathrm{q}}(t)$

$$\vec{r}_{\mathrm{q}}(t) \approx f(t)\vec{r}_{\mathrm{q,CW}}(t).$$

With this, the KH potential $V(\vec{r} - \vec{r}_{\mathrm{q}}(t))$ can be written as the following [87],

$$V_*(\vec{r}, \vec{r}_{\mathrm{q}}, t) = V(\vec{r} - f(t)\vec{r}_{\mathrm{q,CW}}(t)). \tag{3.10}$$

Without any loss of generality, the RHS of Eq. (3.10) can be expanded as

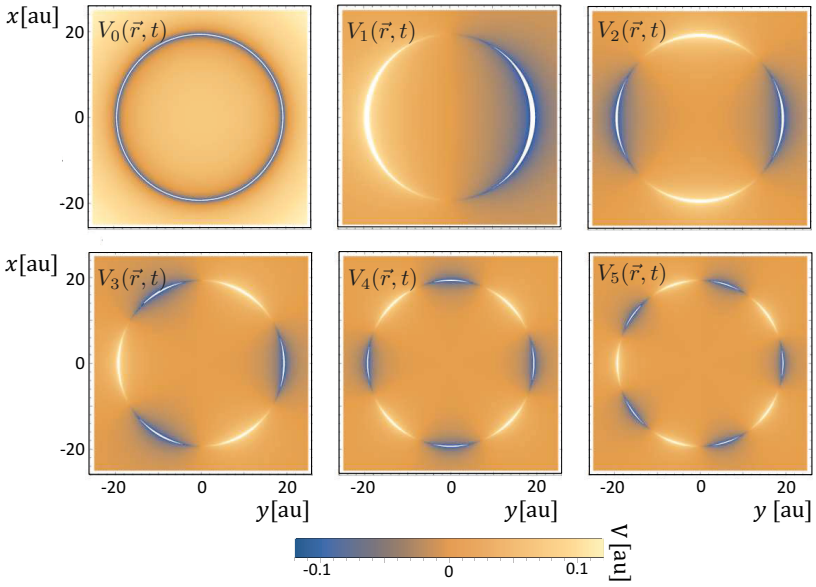

FIGURE 3.3: The first six terms of the series-expansion of potential in the RHS of Eq. (3.13) at time $t = 0$ as a function of x and y coordinate. The laser parameters at work are, ellipticity $\varepsilon = 1.0$, wavelength $\lambda = 800$ nm and intensity $I = 3 \times 10^{14}$ Wcm^{-2}. The radius of the circle is at $r = r_{\rm q} = \dfrac{F_\varepsilon}{\omega^2}$, for the laser parameter used here $r_{\rm q}$ is evaluated as 19.43 au. The white area represents singularity in the potential.

$$V_*(\vec{r},\vec{r}_{\rm q},t) = \int_{-\infty}^{\infty} dt' V(\vec{r} - f(t)\vec{r}_{\rm q,CW}(t'))\delta(t-t'), \tag{3.11}$$

where the pulse-envelope $f(t)$ is kept independent from the integration variable t'.

Now, because of its periodicity of the potential, the above integration in Eq. (3.11) yields the same result if performed only in the interval between $-\pi/\omega$ to π/ω i.e. within one optical cycle duration. Using the properties of the Dirac-delta function,

$$\delta(t-t') = \frac{\omega}{2\pi} + \frac{\omega}{\pi}\sum_{m=1}^{\infty}\cos(m\omega(t-t')), \tag{3.12}$$

in Eq. (3.11), one obtain the following series-expansion

$$V_*(\vec{r},\vec{r}_{\rm q},t) = V_0(\vec{r},t) + \sum_{m=1}^{\infty} V_m(\vec{r},t) \tag{3.13}$$

where

$$V_0(\vec{r},t) = \frac{\omega}{2\pi}\int_{-\pi/\omega}^{\pi/\omega} dt' V(\vec{r} - f(t)\vec{r}_{\mathrm{q,CW}}(t')), \tag{3.14a}$$

$$V_m(\vec{r},t) = \frac{\omega}{\pi}\int_{-\pi/\omega}^{\pi/\omega} dt' V(\vec{r} - f(t)\vec{r}_{\mathrm{q,CW}}(t'))\cos(m\omega(t-t')). \tag{3.14b}$$

The terms $V_m(\vec{r},t)$ are plotted for $t = 0$ and $m = 0,..5$ at Fig. 3.3, having m-fold singularity at a radius $r = r_{\mathrm{q}}$, as can be seen therein.

The total force exerted on the ionized electron is calculated by taking the radial derivative of the potential, i.e.,

$$f_r = -\frac{\partial V_*}{\partial r}, \tag{3.15}$$

and Newton's equations of motion for the force f_r are solved to get the electron trajectories in Fig. 3.4. Although the exact KH trajectory is reproduced in the combination of just the first two terms (m = 0,1), it already agrees reasonably with the trajectory in the zeroth-order term (m = 0).

The zeroth-order term $V_0(\vec{r},t)$ is almost time-independent. The time-dependence only comes through the slowly varying $f(t)$. That the trajectory in $V_0(\vec{r},t)$ is close to the exact one, motivates us to explore the problem from a time-independent perspective. In the following, we study the complete cycle-average of the KH potential and discuss its validity for different laser intensities.

3.2.3 Trajectory in the cycle-averaged KH potential

In this section, we consider the total KH potential averaged over a full optical cycle, and therefore analyse the electron dynamics in such a complete time-independent problem. In the following, we derive an analytical expression for the cycle-averaged KH potential in the presence of a circularly-polarized (CP), CW laser pulse.

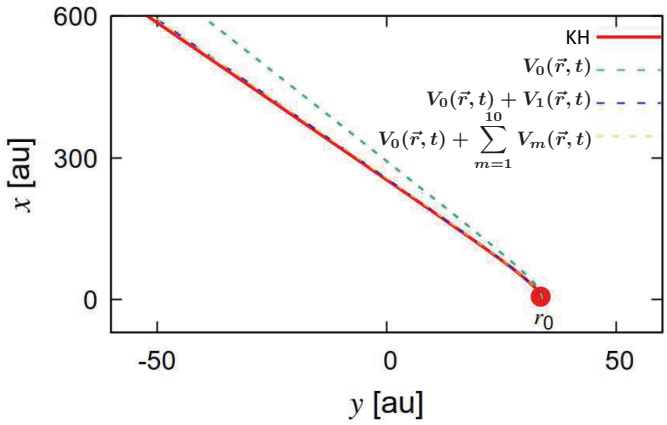

FIGURE 3.4: Electron trajectory in the exact KH potential (red solid curve), for the zeroth-order term $V_0(\vec{r},t)$ of the series-expansion in Eq. (3.13) (green dashed curve), in the combination of the first two terms in that expansion i.e. $V_0(\vec{r},t)+V_1(\vec{r},t)$ (blue dashed curve), and in the first eleven terms i.e. $V_0(\vec{r},t)+\sum_{m=1}^{10}V_m(\vec{r},t)$(yellow dashed curve). The trajectory in the potential up to the 10th-order term and up to 1st-order term in the series-expansion Eq. (3.13) are indistinguishable in the figure. The intensity is $I=10^{14}$ Wcm^{-2}. Other parameters are the same as in Fig. 3.2. The initial point is represented by the circle.

The KH potential reads

$$\begin{aligned} V(\vec{r},\phi) &= -\frac{1}{\mid \vec{r}-\vec{r}_{\mathrm{q,CW}}(\phi)\mid} \\ &= -\frac{1}{\sqrt{(x-r_{\mathrm{q}}\sin(\phi))^2+(y-r_{\mathrm{q}}\cos(\phi))^2}}, \end{aligned} \tag{3.16}$$

with $\vec{r}_{\mathrm{q,CW}}(\phi)$ from Eq. (3.3) for ellipticity $\varepsilon=1.0$ and phase $\phi=\omega t$.

The cycle-averaged KH potential, in this case, is expressed as

$$\begin{aligned} V_0(\vec{r},r_{\mathrm{q}}) &= -\frac{1}{2\pi}\int_0^{2\pi} d\phi \frac{1}{\sqrt{(x-r_{\mathrm{q}}\sin(\phi))^2+(y-r_{\mathrm{q}}\cos(\phi))^2}} \\ &= -\frac{1}{2\pi}\int_0^{2\pi} d\phi \frac{1}{\sqrt{r^2+r_{\mathrm{q}}^2-2rr_{\mathrm{q}}\cos(\phi-\theta)}}, \\ &= -\frac{2}{\pi\tilde{r}}K(a). \end{aligned} \tag{3.17}$$

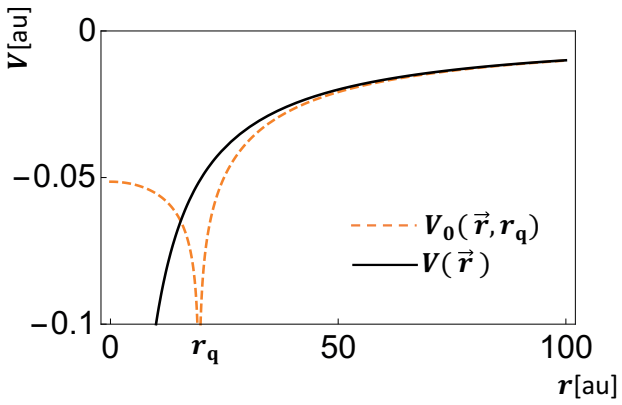

FIGURE 3.5: The cycle-averaged KH potential (dashed orange curve) $V_0(\vec{r}, r_q)$ Eq. (3.17) as a function of r. The laser parameters are intensity $I = 3 \times 10^{14}$ Wcm^{-2}, ellipticity $\varepsilon = 1.0$, and wavelength $\lambda = 800$ nm for He atom. V_0 has a singularity at $r = r_q$, for the current parameters, which is equal to 19.43 au. The Coulomb potential is shown as a solid black curve.

Here θ is the polar angle corresponding to the electron trajectory. This is nothing but $V_0(\vec{r}, t)$ in Eq. (3.13) for a CW pulse with $f(t) = 1$. Here,

$$\tilde{r} = r + r_q, \tag{3.18}$$

$$a = \frac{4rr_q}{\tilde{r}^2}. \tag{3.19}$$

K is the elliptic integral of the first-kind. The above potential has a singularity at $r = r_q$ since K diverges for $a = 1$, this can be also seen from Fig. 3.5 (see also [33, 34, 88]).

In Fig. 3.6, the most-probable electron trajectory, i. e., the trajectory at the field-maximum, which occurs at $t = 0$, cf. Eqs. (2.6)-(2.7), is compared within the exact KH problem and in V_0 (Eq. (3.17)) for intensities $I = 8\times10^{13}$ Wcm^{-2} and $I = 8\times10^{14}$ Wcm^{-2}. We can see that the electron trajectory in V_0 follows the real KH trajectory for the lower intensity. However, for the higher intensity, the former deviates from the latter. The reason behind this is discussed in the following.

The quiver amplitude r_q, which also represents the maximum extension of the KH potential, is proportional to the field-amplitude F_{max}, whereas the exit-radius r_e is inversely proportional to it (Eq. (E.2)). Therefore, for the low-intensity pulse, $r_q \ll r_e$, which can be also seen from Fig. 3.6(a). As a result, the electron's initial position is much larger

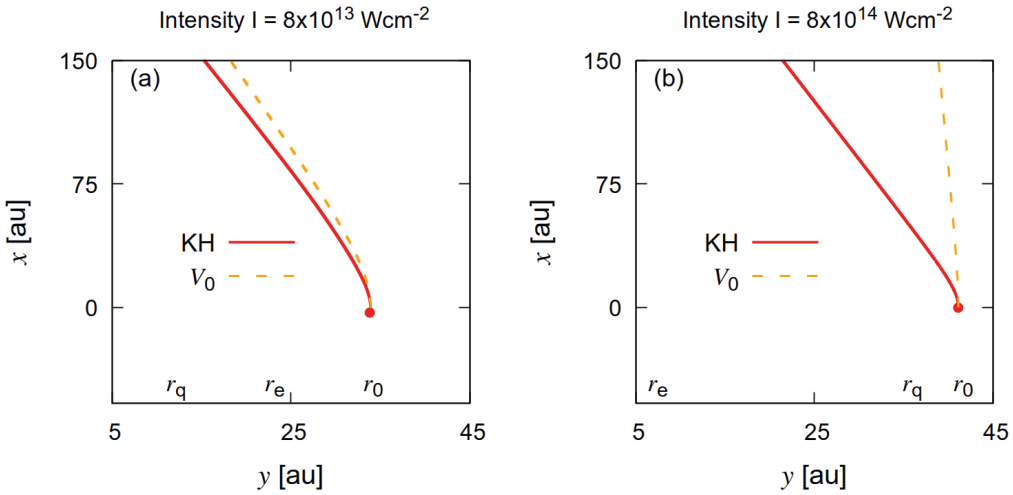

FIGURE 3.6: The most-probable trajectory of the electron, for two different laser intensities. The solid red curve is the real time-dependent KH trajectory whereas the orange dashed curve corresponds to the electron trajectory in the time-independent cycle-averaged KH potential Eq.(3.17). The parameters at work are ellipticity $\varepsilon = 1.0$ and wavelength $\lambda = 800$ nm for He atom. The initial point is represented by the circle.

than r_q, i. e., $r_0 = r_e + r_q \gg r_q$, cf. Eq. (3.9). This means that the electron trajectory is far away from the singularity, so the real dynamics is indistinguishable from the corresponding cycle-averaged motion. On the other hand, for the high intensity, r_q becomes much larger than r_e (see Fig. 3.6(b)), resulting in $r_0 \approx r_q$. Since the electron is released very close to the KH potential, the cycle-averaged approximation does not hold anymore, leading to the deviation, as observed in Fig. 3.6(b).

In the following sections, we will analyse the deviation and discuss the new static potential to compensate for the deviation.

3.3 Conserved quantities in the KH problem

To investigate the possible static potential, we need a suitable reference to start with. For that, in the first place, one can think of a Kepler problem. The following field-free Hamiltonian drives the corresponding electron trajectory

$$H(\vec{r}, \vec{p}, t) = \frac{\vec{p}^{\,2}}{2} + V(\vec{r}). \tag{3.20}$$

At distances $r \gg r_{\mathrm{q}}$, the KH problem cf. Eq. (3.8) becomes a Kepler's problem. Therefore, it is interesting to see how the quantities known to be conserved in the latter are actually behaving for the former.

The conserved quantities in a Kepler problem are the energy E, angular momentum l, and the Runge-Lenz vector (RLV) $\vec{a}$,

$$E = \frac{\vec{p}^2}{2} + V(\vec{r}), \tag{3.21a}$$

$$l_z = (\vec{r} \times \vec{p})_z, \tag{3.21b}$$

$$\vec{a} = \vec{p} \times \vec{l} - \vec{r}/r. \tag{3.21c}$$

The angular momentum $\vec{l}$ points along the z-axis, perpendicular to the plane of polarization (xy-plane). The RLV $\vec{a}$ lies in the plane of polarization with the angle $\alpha = \tan^{-1}(\frac{a_x}{a_y})$ relative to the major axis. The absolute value of $\vec{a}$ is given by the eccentricity of the Kepler hyperbola, which reads $|a| = \sqrt{1 + 2El^2}$.

At the end of the laser pulse, these three quantities are conserved. Starting from the phase-space coordinates when the pulse is gone, which are obtained by forward propagating the KH trajectory, we back-propagate in time in the KH Hamiltonian until the release time t_0. E, l, and $\vec{a}$ as a function of time are shown in Fig. 3.7.

One can observe an interesting behaviour in these quantities for different laser-intensities. E and l hardly change as a function of time for all the intensities Fig. 3.7(a)-(b). In contrast, the RLV angle α remains almost constant for lower intensity and changes significantly for the higher intensity. The change in α occurs within a concise duration after the release time t_0 (here $t_0 = 0$ for the most-probable trajectory). Then it gets saturated within a time $t \ll T$, as shown in Fig. 3.7(c). Later we will see, this change within such a short time helps to formulate a static potential by performing a series-expansion.

For the low intensity, all the three quantities E, l, α, which are conserved in a Kepler problem, are also approximately constant for a KH trajectory. We will see in section 3.4.2, the real trajectory is nicely captured within the Kepler problem. For the high

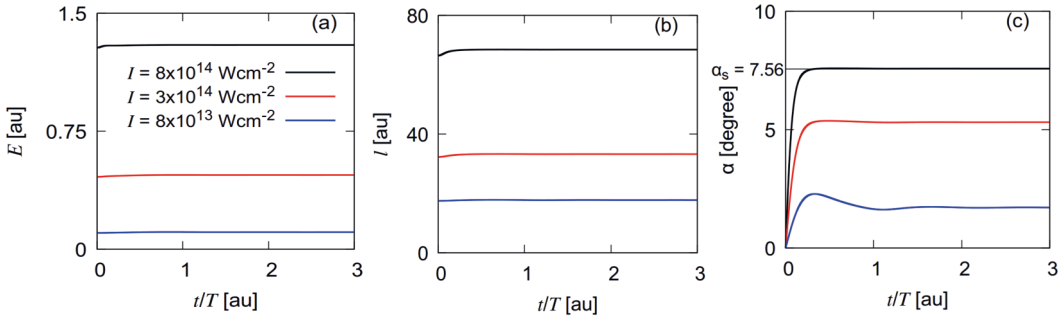

FIGURE 3.7: Energy E, angular momentum l, and the RLV angle α as a function of time for three different laser intensities $I = 8 \times 10^{14}$ Wcm^{-2} (black curve), $I = 3 \times 10^{14}$ Wcm^{-2} (red curve), and $I = 8 \times 10^{13}$ Wcm^{-2} (blue curve) for electron's trajectory in the KH Hamiltonian Eq. (3.1). The laser parameters other than intensity at work are the ellipticity $\varepsilon = 0.8$, wavelength $\lambda = 800$ nm for He atom.

intensity, since α changes with time, keeping E, l almost constant, leading us to construct a rotation in the Kepler trajectory. The rotated Kepler trajectory agrees with the present observation, as will be discussed in section 3.4.2.

Most importantly, the energy E (Eq. (3.21c)) is almost constant in time for all the intensities, motivating us to formulate a time-independent Hamiltonian, which is discussed in the next section. Moreover, the angular momentum's conservation indicates a spherically symmetric potential, which will be taken into account for the new static potential.

3.4 Formalism of a time-independent problem

This section discusses the formalism of a time-independent problem that can capture the post-tunnelling dynamics in the presence of an elliptically-polarized laser pulse Eq.(2.7).

3.4.1 Static ring potential

The RLV angle α changes very quickly and becomes constant as can be seen from Fig. 3.7, indicating that the electron experiences the time-dependence of the KH potential for a short duration after its release. It flies away quickly so that we can use a short-time

expansion. Before going into that, we need the initial coordinates of the electron after tunnelling in the KH potential.

To do so, we recall the initial angular momentum of the electron,

$$\vec{l_0} = \vec{r_0} \times \vec{p_0}. \tag{3.22}$$

According to Eq. (3.9), the initial momentum for the laser pulse Eq. (2.7) with $\vec{p}_e = 0$ and $\vec{p}_\mathrm{q}$ from Eq. (3.6) is given by

$$\begin{aligned} \vec{p}_0 &= -\vec{A}(t_0 = 0) \\ &= \frac{F_\varepsilon \varepsilon}{\omega} \vec{e}_x. \end{aligned} \tag{3.23}$$

The initial position is given by

$$\begin{aligned} \vec{r}_0 &= \vec{r}_e + \vec{r}_\mathrm{q}(t_0 = 0) \\ &\approx r_\mathrm{q}\ \vec{e}_y = \frac{F_\varepsilon}{\omega^2}\ \vec{e}_y. \end{aligned} \tag{3.24}$$

The last approximation can be made for high-intensity laser pulses i. e. $|\vec{r}_e| \ll |\vec{r}_\mathrm{q}|$. Here, $\vec{r}_\mathrm{q}(0) = r_\mathrm{q}\ \vec{e}_y$, as calculated for the easiest case of a CW pulse in Eq. (3.3). Using Eqs. (3.23) and (3.24) in Eq. (3.22) we obtain,

$$l_0 = \frac{F_\varepsilon^2 \varepsilon}{\omega^3}. \tag{3.25}$$

In polar coordinates l_0 is given by

$$l_0 = r_0^2 \dot{\theta_0}. \tag{3.26}$$

Comparing this equation with Eq. (3.25) with r_0 from Eq. (3.24), the following equality is found

$$\theta_0 = \varepsilon \omega t. \tag{3.27}$$

Now, for a very short time after release, i. e., for $t \gtrsim t_0$, the above equation can be approximated as

$$\tan\theta = \varepsilon \tan\phi, \tag{3.28}$$

where θ is the polar angle of the electron's trajectory, and $\phi = \omega t$ is the phase of the KH potential. Next we will use this short time relation within the KH potential.

The KH potential with $f(t) = 1$ for a CW laser pulse is given by

$$V(\vec{r}, \phi) = -\frac{1}{\sqrt{(x - r_{\mathrm{q}}\, \varepsilon \sin(\phi))^2 + (y - r_{\mathrm{q}} \cos(\phi))^2}}. \tag{3.29}$$

Using the following short-time relations, derived from Eq. (3.28)

$$\sin\phi = \frac{x}{\sqrt{x^2 + y^2\varepsilon^2}}, \qquad \cos\phi = \frac{y\varepsilon}{\sqrt{x^2 + y^2\varepsilon^2}} \tag{3.30}$$

in Eq. (3.29), the following static potential results

$$V_{\mathrm{s}}(x, y, r_{\mathrm{q}}, \varepsilon) = -\frac{1}{\sqrt{\dfrac{x^2 + y^2}{y^2\varepsilon^2 + x^2}\left(\sqrt{y^2\varepsilon^2 + x^2} - r_{\mathrm{q}}\varepsilon\right)^2}}. \tag{3.31}$$

For near circularly-polarized laser pulses, i. e., $\varepsilon \to 1$, the above static potential reduces to the following ring potential, which has a Coulomb singularity on a ring at $|\vec{r}| = \sqrt{x^2 + y^2} = r_{\mathrm{q}}$, given by

$$V_{\mathrm{ring}}(\vec{r}, r_{\mathrm{q}}) = -\frac{1}{|\,\vec{r}\,| - r_{\mathrm{q}}}. \tag{3.32}$$

This ring potential is very similar to the cycle-averaged KH potential. Both have a singularity at $r = r_{\mathrm{q}}$. However, the types of singularities are different.

The ring potential makes a smooth transition to the Coulomb potential $V(\,\vec{r}\,) = 1/|\,\vec{r}\,|$ for distances $r \gg r_{\mathrm{q}}$ i. e. for $t \gg t_0$, and this is also expected from the exact KH potential. Therefore, the exact dynamics is reproduced within the ring potential nicely, as shown in Fig. 3.8(a). The asymptotic angle $\theta(\infty)$ as obtained from the static potential V_s cf. Eq. (3.29), is compared within the KH problem which is shown in Fig. 3.8(b). For nearly CP pulses, both angles agree well with each other. However, for ellipticities smaller than 1, the final angle captured in the static potential deviates from the KH angle. The deviation increases with decreasing ellipticity. The reason for the deviation for the low ellipticities is the low initial velocity of the electron. Since it does not leave the the parent ion quickly, the short-time expansion fails.

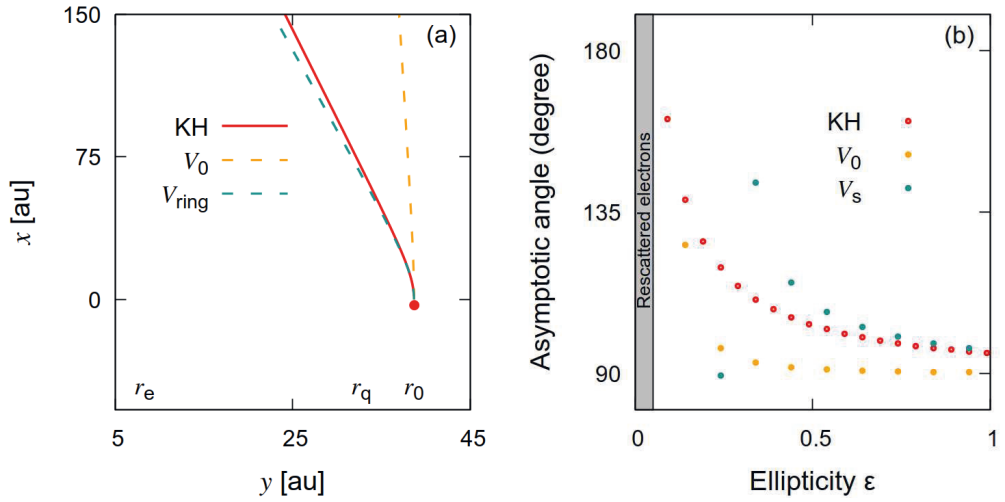

FIGURE 3.8: Left panel (a): the most-probable trajectory of the electron, for the parameters as in Fig. 3.6(b). The real KH trajectory (red solid curve) is reproduced in the ring potential (dark-green dashed curve), whereas the trajectory in the cycle-averaged KH potential, cf. Eq. (3.17) deviates from the real trajectory. Right panel (b): the final angle of the electrons as a function of ellipticities in all the three potentials namely time-dependent KH (red circles), cycle-averaged KH potential V_0 (orange points), and the new static potential V_s (dark-green points), cf. Eq. (3.29). The wavelength and intensity used here are respectively $\lambda = 800$ nm, and $I = 8 \times 10^{14}$ Wcm^{-2} for the He atom.

The final angle of the electron is close to 90 degree for high ellipticities. Since the field amplitude at the release time t_0 is smaller for the higher ellipticities than for the lower ones, the tunnel exit-radius becomes larger for the former, and consequently, the Coulomb attraction force at the exit becomes smaller. This results in almost no deviation from the 90-degree angle as expected from the SFA problem, i. e., ignoring the Coulomb attraction force.

In the following a rotated Kepler problem is introduced, which shows that a time-independent formalism can estimate the electron's final angle for a larger range of ellipticities.

3.4.2 A rotated Kepler problem

In a Kepler problem, the particle's trajectory in the presence of a Coulomb attractive force $V(r)$ is defined by the energy E, the angular momentum l of the particle, and the

position of the closest approach, which is given by the expression [89]

$$r(\theta) = \frac{l^2}{1 + \sqrt{1 + 2El^2}\cos(\theta)}, \tag{3.33}$$

where r, θ are polar coordinates.

The Kepler trajectory Eq. (3.33) is plotted in Fig. 3.9. Figure 3.9(a) shows that the electron trajectory in the real KH problem does not deviate much from the Kepler trajectory, for intensity $I = 8 \times 10^{13}$ Wcm^{-2}. This is expected for such a low intensity, since the energy E, angular momentum l, and RLV angle α are approximately conserved, as discussed in section 3.3. Here, we have used E and l, as the initial values (at time $t = t_0$) E_0, and l_0 respectively, since they are approximately constant (see Fig. 3.7(a)-(b)).

However, from Fig. 3.9(b) for intensity $I = 8 \times 10^{14}$ Wcm^{-2}, we can see the KH trajectory deviates from the Kepler trajectory. This deviation is expected since the RLV angle α changes significantly for such high intensity (Fig. 3.7(c)). Since the RLV angle is directed along the major axis of any Kepler trajectory, to account for the change in α for the real KH trajectory, we consider a rotation around the major axis by α_s, where α_s is the saturation value of α as denoted in Fig. 3.7(c). This rotation is consistent with the observation that E and l are approximately conserved. The rotated Kepler trajectory therefore takes the form

$$r(\theta) = \frac{l^2}{1 + \sqrt{1 + 2El^2}\cos(\theta - \alpha_s)}. \tag{3.34}$$

For a CP pulse with $\varepsilon = 1$, wavelength $\lambda = 800$ nm, and intensity $I = 8 \times 10^{14}$ Wcm^{-2},

$$\alpha_s = 7.56^\circ$$

which is also denoted in Fig. 3.7(c). Using this value of α_s with $E = E_0$, $l = l_0$ calculated at time $t = t_0 = 0$, the rotated Kepler trajectory, cf. Eq. (3.34), as plotted in Fig. 3.9(b), lies very close to the real KH trajectory.

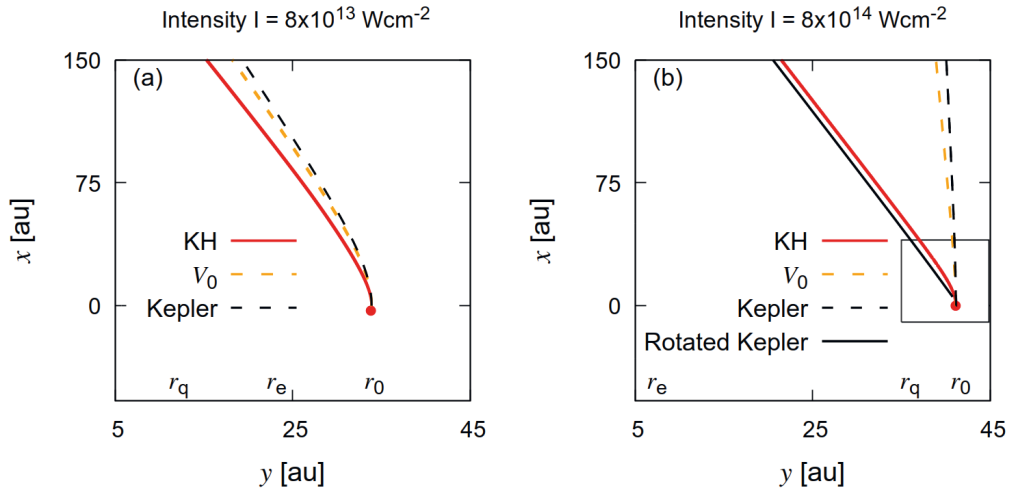

FIGURE 3.9: The most-probable trajectory of the electron, for two different laser intensities — (a) $I = 8 \times 10^{13}$ Wcm^{-2}, and (b) $I = 8 \times 10^{14}$ Wcm^{-2} . The red curve is the real time-dependent KH trajectory whereas the orange curve corresponds to the electron trajectory in the time-independent cycle-averaged KH potential Eq.(3.17). The black dashed and solid curve in these figures correspond to the Kepler trajectory, cf. Eq. (3.33) and the rotated Kepler trajectory, cf. Eq. (3.34), respectively. The parameters are ellipticity $\varepsilon = 0.8$ and wavelength $\lambda = 800$ nm for He atom. The initial point is represented by the circle. See the text for the other details. The rectangular segment within (b), is shown in Fig. 3.10.

In Fig. 3.10, this slight change in the direction of the closest approach can be noticed very clearly. So we can see from this figure that the Kepler trajectory, cf. Eq. (3.33), which is the same as $\alpha_s = 0$ in Eq. (3.34), deviates from the real trajectory. However, by making a slight change in the closest approach of the Kepler trajectory, i. e., changing $\alpha_s = 0$ to $\alpha_s = 7.56°$ in Eq. (3.34), takes the trajectory very close to the real time-dependent KH trajectory.

In Fig. 3.11, the α_s, which are obtained as the RLV angles at the end of the laser pulse from a KH problem, are plotted as a function of ellipticity ε. For all intensities, α_s decreases with increasing ε. Since the field maximum at the tunnel exit becomes smaller as we increase ε, hence the exit radius r_e becomes larger, which makes the rotation angle smaller for the higher ellipticities. α_s has been fitted with the function

$$\alpha_s(\varepsilon) = b/\varepsilon, \tag{3.35}$$

with b being the fitting parameter.

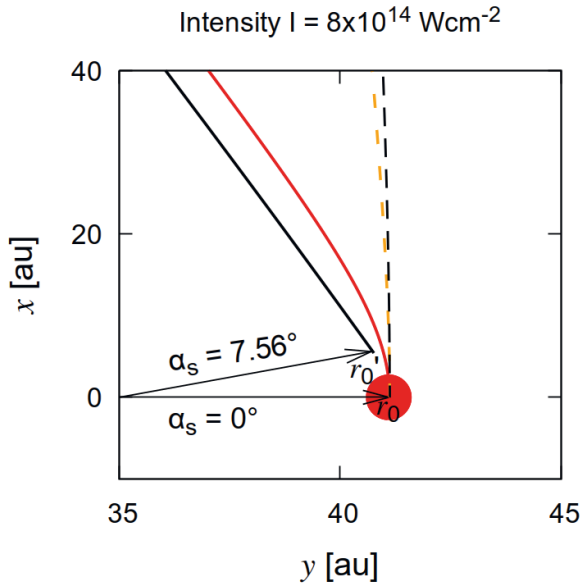

FIGURE 3.10: The zoomed segment from Fig. 3.9(b). The arrows represent the direction of the final RLV angle α_s, which is also the closest approach of the corresponding Kepler trajectory. $\alpha_s = 0°$ for the Kepler trajectory, cf. Eq. (3.33), and $\alpha_s \neq 0$ for the rotated Kepler, cf. Eq. (3.34) with the value $\alpha_s = 7.56°$.

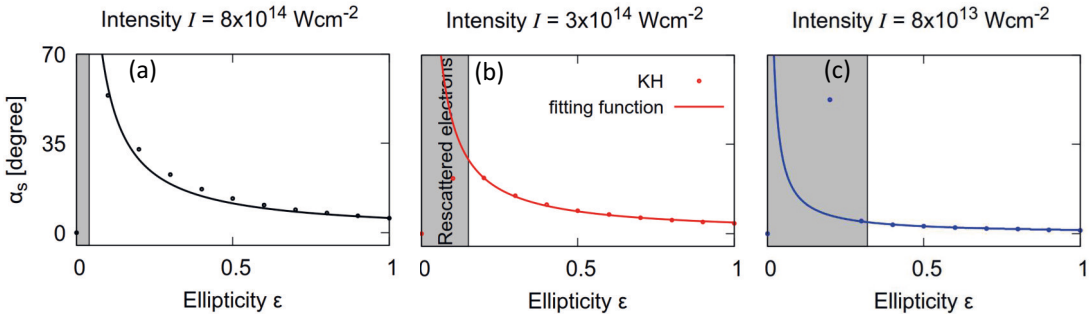

FIGURE 3.11: Final RLV angle α_s as a function of ellipticty ε for three different laser intensities. The wavelength λ used here is 800 nm for He atom. The points are the RLV angle α obtained in a KH problem at the end of the laser pulse and the solid curves are the corresponding fitting functions, cf. Eq. (3.35) with the fitting parameter $b = 5.7°$ for intensity $I = 8 \times 10^{14}$ Wcm^{-2} in (a), $b = 4.3°$ for intensity $I = 3 \times 10^{14}$ Wcm^{-2} in (b), and $b = 1.4°$ for intensity $I = 8 \times 10^{13}$ Wcm^{-2} in (c).

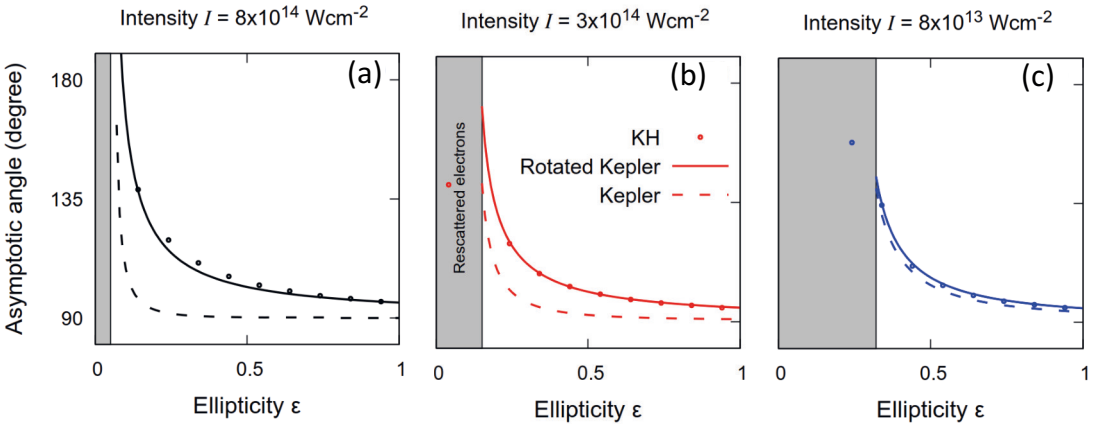

FIGURE 3.12: The asymptotic angle as a function of ellipticity for three different laser intensities. The angle obtained from the KH problem is plotted with points, the solid curve corresponds to the rotated Kepler problem as described in the text, and the dashed curves are the angle from a pure Kepler problem.

We notice that the values of b decrease with intensity, and for the lowest value of intensity here, i. e., for $I = 8 \times 10^{13}$ Wcm^{-2}, this value is close to zero (the numerical values are given in the figure caption. For this intensity, $b = 1.4°$). This is expected from our observation of the zero rotation-angle needed to reproduce the KH problem by a Kepler problem for such low-intensity.

Figure 3.12 compares the electron's final angle in the KH problem and a rotated Kepler problem. For the latter, we have propagated the electron trajectory in a Kepler problem, but not with the KH initial conditions $\vec{r}_0, \vec{p}_0$, but with $\vec{r}_0{}', \vec{p}_0{}'$ translated into the rotated coordinate system. If the coordinate system is rotated by α_s, the coordinate values in the new frame are obtained by a rotational transformation with the angle -α_s,

$$\vec{r}_0{}' = R_{-\alpha_s}\vec{r}_0 \qquad\qquad \vec{p}_0{}' = R_{-\alpha_s}\vec{p}_0. \tag{3.36}$$

This transformation is illustrated in Fig. 3.10. The final angle is reproduced within such a rotated Kepler problem with α_s from Eq. (3.35) for all the ellipticities and intensities, as shown in Fig. 3.12.

3.5 Summary

In this chapter we formulated a time-independent formalism that can reproduce the exact field-driven electron dynamics. The classical electron trajectory is separately solvable in the presence of an oscillatory laser (Simple-man's model) or in the presence of the Coulomb interaction (Kepler problem). However, in the combined presence of both it is difficult to solve. Usually, the strong-field driven dynamics is approximated by the SMM only, considering that the Coulomb force can be neglected as compared to the strong laser force. This is not adequate in an attoclock setup. For near CP pulses, the Coulomb asymmetry plays a crucial role that can not be ignored [18]. Alternatively, separating the fast laser oscillations from the Coulomb scattering has led to interesting recent theories [35, 36, 90]. In [35, 36], e. g., the motion-averaged effective potential turned out to be a pure Coulomb potential which can approximate the real electron dynamics. However, the theory is only valid for low intensities in the weak-tunnelling regime. This is consistent with the Keldysh-Rutherford model, which has found the final attoclock offset angle using only a Rutherford scattering problem showing agreement in the weak-tunnelling regime only [37]. In the framework of the KH potential, the electron trajectory can be described exactly. Since for large distances the KH potential becomes a Coulomb potential, and since in the weak-tunnelling regime, the electron is always far away from the nucleus, both of the above theories [35, 37] are plausible. However, for the strong-tunnelling regime, the electron initially stays close to the moving KH potential and then quickly moves away after release. Therefore a short-time expansion within the KH potential leading to an unconventional static ring potential, with Coulomb singularity at a ring of radius equated to the quiver amplitude, reproduces the real dynamics. Moreover, the short-time behaviour of the conserved quantities of a Kepler problem associated with the KH trajectory leads to a change in the RLV. This change has been encountered in a rotated Kepler problem providing the time-independent formalism of electron dynamics for a broader parameter region.

Chapter 4

Analytical prediction of the attoclock angle

4.1 Introduction to attoclock

Attosecond angular streaking [7] or the"attoclock" is a new and compelling technique to probe the microscopic time-resolved dynamics of electrons. When atoms and molecules are subjected to intense, nearly circularly-polarized laser pulses, the electrons that are ionized at different times of the corresponding electric field reach the detector at different deflection angles in the photo electron-momentum plane. This angle can be mapped to time. Such a method can elucidate various temporal properties of the electrons such as photo-emission and photo-absorption time delay, tunnelling time of an electron through an atomic potential barrier, and may also resolve the reaction time of various chemical and optoelectronic processes with attosecond time resolution.

An attoclock experiment was performed for the first time by Eckle *et al* in the year 2008 [8]. A Titanium:Sapphire-based laser system is used to produce an elliptically, in particular nearly circularly-polarized laser pulse characterized by a center wavelength of 725 nm with a duration of 2 optical cycles. Such a short and intense laser pulse is focused onto helium atoms and with the cold target recoil ion momentum spectroscopy (COLTRIMS) apparatus, the photo electron-momentum distribution (PMD) of the ions generated during the laser-atom interaction is measured [91]. Due to the conservation

of momentum, the PMD of the electrons is essentially a reflection of the corresponding PMD of the ions (Fig. 4.1), from which the electrons were ionized.

To gain further insight into the dynamics of the ejected electron from the atom and to study the relevant observables, we illustrate the underlying principles and discuss the elementary measurement procedures in a typical attoclock experimental setup below.

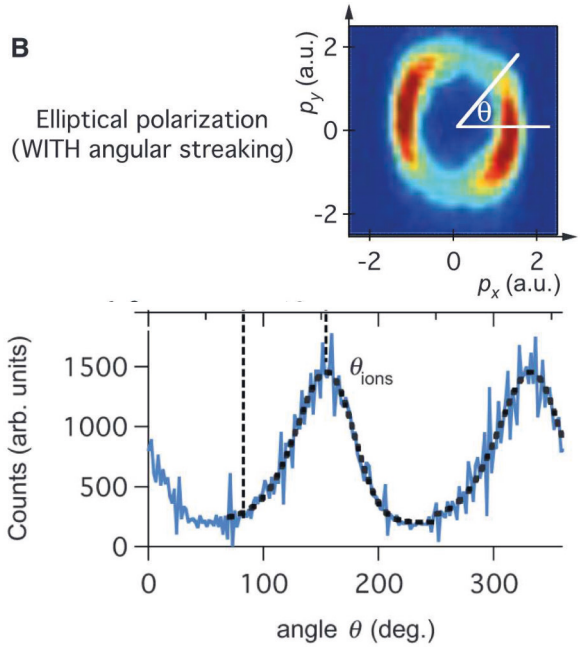

FIGURE 4.1: First attoclock experimental results from Eckle *et al* [8]. This experiment uses a nearly circularly-polarized laser which is polarized in the xy plane. *Top panel*: Photo-electron momentum distribution (PMD). Two symmetric lobes are observed in the PMD. The attoclock offset angle is defined as the polar angle θ in the photo-electron momentum plane at which the PMD shows maximum. *Bottom panel*: The angular spectra is obtained as the yield as a function of θ. The observed peaks correspond to the two symmetrically placed maximums of the PMD, and therefore are separated by an angle 180°. Typically the angle corresponding to one of these maximums is the measure of the offset angle. Figure is taken from Eckle *et al* [8].

4.2 State-of-the-art measurement and attoclock angle

Within the strong-field approximation (SFA), the vector potential corresponding to the laser field is imprinted on the momentum of the photoelectron, cf. Eq. (2.23). For the context of the attoclock, the vector potential $\vec{A}(t)$ for an elliptically-polarized laser pulse

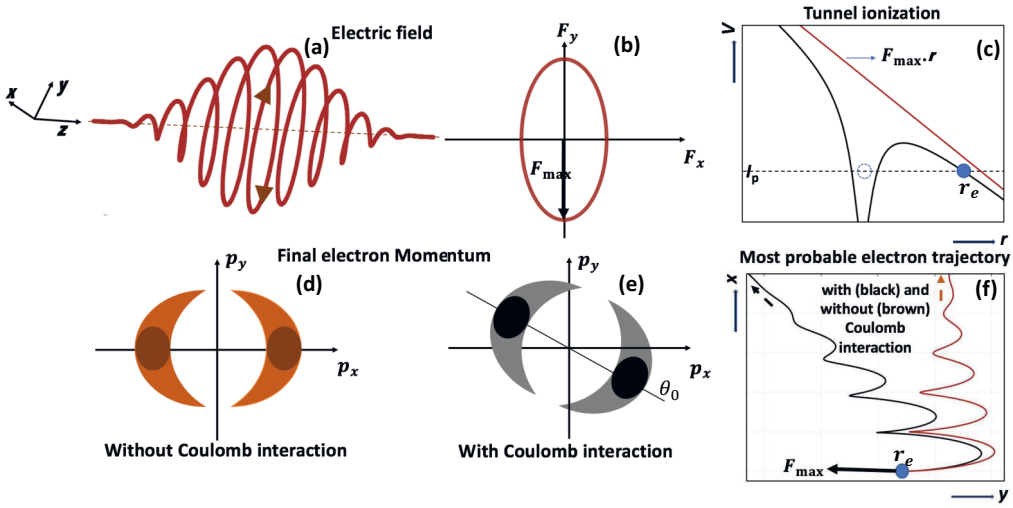

FIGURE 4.2: Clockwise-rotating electric field vector of an elliptically-polarized laser (Eq. (2.6)) (a), its projection in the xy plane with the maximum of the field vector pointing along the negative y axis (b) and the tunnel ionization of an electron in an atomic potential at the instantaneous electric field maximum $F_{\max}$ (brown solid line) (c). $I_{\rm p}$ is the ionization potential and r_e is the radial coordinate of electron at the ionization time. The bottom row shows the schematic of the final PMD without (d) and with (e) Coulomb interaction. The highest probability of tunnelling is reached at the peak of the electric field and this corresponds to the most-probable electron trajectory which is shown in (f).

with a clockwise-rotating electric field is defined by Eq. (2.7). The asymptotic momentum of the electron which is measured at the detector can be obtained within the SFA by using Eq.(2.25) at $t \to \infty$, and for a finite-duration laser pulse this yields

$$\vec{p}(t \to \infty) = \vec{A}(t_0), \tag{4.1}$$

where, the final momentum depends only on the vector potential at the time of electron release t_0. This means that the electrons ionized at different ionization times reach the detector with different asymptotic momentum.

Equation (4.1) does not take care of the Coulomb interaction of the ionized electron with the parent-ion. However, in a realistic scenario, the presence of the Coulomb interaction can give rise to an interesting shift of the final momentum of the electron given by Eq. (2.26). The corresponding deflection angle in the photo electron-momentum plane

depends on the ionization time t_0

$$\theta(t_0) = \tan^{-1}\left(\frac{p_y(t\to\infty)}{p_x(t\to\infty)}\right), \tag{4.2}$$

with p_y and p_x are the y and x component of the momentum in Eq. (2.26), respectively.

The schematic in Fig. 4.2 illustrates the above mentioned basic principles and measurement procedures. Figure. 4.2(a) shows the electric field of the elliptically-polarized laser pulse in Eq.(2.7), propagating along the z-axis. The projection of this laser pulse in the xy plane of polarization is depicted in Fig. 4.2(b). The major-axis of polarization is along the y-axis, as also can be seen from Eqs.(2.6)-(2.7). The bound electron is released from the atom by tunnel ionization within a quasi-static scenario, and the most-probable electron trajectory is generated by the instantaneous field-maximum $F_{\max}$. The corresponding effective potential is sketched in Fig. 4.2(c). It can be seen from Fig. 4.2(d) that the PMD is distributed at a perpendicular direction with respect to the applied electric field vector Fig. 4.2(b) without including the Coulomb interaction, which follows also immediately from Eq. (4.1). Including the Coulomb interaction, leads to a PMD, tilted by an angle (see Fig. 4.2(e)). This deflection angle can be calculated by using Eq. (4.2).

The angle at the maximum of the PMD corresponding to the most-probable trajectory ($t_0 = 0$) is also sometimes called the offset angle, which is then given by

$$\theta_0 = \theta(t_0 = 0). \tag{4.3}$$

Therefore, θ_0 is the angle by which the maximum of the PMD is tilted with respect to the polarization ellipse's major axis as shown in Fig. 4.2(e). However, for a circularly-polarized laser pulse, there is no preferred direction, rather the electrons are distributed uniformly on a circle for a CW laser or a long laser pulse. To obtain θ_0, one requires a laser pulse with a short duration (few optical cycles, say one or two) in this case. Since the pulse is short, the ionization amplitude is relevant at the peak of the electric field-amplitude corresponding to the first optical cycle only and falls rapidly with time. Therefore, the uniformity is destroyed, and a preferred direction is obtained from which the offset angle is calculated. However, a real experiment deals with near circularly-polarized laser without the requirement of such short pulses.

In [92, 93], the offset angle θ_0 is mapped to the tunnelling time , i. e., the time-span an electron spends under an atomic potential barrier, which is a classical forbidden region. The time-delay can be obtained by using the following formula [81]

$$\Delta\tau(t_0) = \frac{\theta_0}{\omega}. \tag{4.4}$$

However, finite tunnelling times and their determination through the attoclock is one of the most discussed controversial topics in strong-field physics [22, 25–28, 37, 41, 42].

Here, we study the post-ionization dynamics of electron starting from the tunnel exit. The dynamics in this region can be described classically. The electrons can not come close to the parent-ion in the presence of the near circularly-polarized laser pulse in the attoclock experimental setup. Therefore, they can not re-scatter or re-collide with the parent-ion. Rather they are directly ionized and reach the photo electron-momentum plane with a finite asymptotic angle. In the subsequent sections, we will focus on the calculations of θ_0, cf. Eq. (4.3). Intriguingly, we have found an approximated analytical expression for this angle, as discussed in section 4.4. It should be noted that there have been attempts to achieve the goal using different approaches, which can be found in [20, 37, 83].

We will discuss the derivation of our analytical angle and show its nice agreement with the numerical results obtained from the classical-trajectory Monte Carlo simulations as well as with the available experimental data [21, 23, 94].

4.3 Classical-trajectory Monte Carlo simulations

To understand the tunnel-ionized electron dynamics, we adopt the classical-trajectory Monte Carlo (CTMC) [17, 39, 95] simulation procedure. In this method, electron trajectories are simulated by solving classical equations of motion with a selective distribution of initial phase-space coordinates.

4.3.1 Classical propagation

We describe the dynamics of the tunnel-ionized electrons in the combined effect of the laser force and Coulomb attraction in the length-gauge. Within single-active-electron (SAE) approximation and dipole approximation, the corresponding Hamiltonian is given by Eq. (2.15).

We solve Hamilton's equations of motion for this Hamiltonian. The numerical integration is performed using the leap-frog algorithm [96]. The electron trajectories are propagated until the end of the laser pulse, where the problem becomes a Kepler problem. In such a problem, there are three constants of motion, which are respectively, the angular momentum $\vec{l} = \vec{r} \times \vec{p}$, the Runge-Lenz vector (RLV) $\vec{a} = \vec{p} \times \vec{l} - \vec{r}/r$, and the energy $E = \vec{p}^2/2 - 1/r$. Here, $\vec{r}$ and $\vec{p}$, respectively, are the position and momentum at the end of the pulse.

The asymptotic momentum $\vec{P}$, which is typically measured at the detector, is given by

$$\vec{P} = P\frac{P(\vec{l} \times \vec{a}) - \vec{a}}{1 + P^2\vec{l}^2}. \tag{4.5}$$

The magnitude P can be evaluated using the conservation of energy, i. e.,

$$P^2/2 = \vec{p}^2/2 - 1/r. \tag{4.6}$$

The details of the derivation of Eq. (4.5) is given in appendix B.

The details of the initial conditions and the calculations of the relevant observable measured in an attoclock setup are provided below.

4.3.2 Initial conditions

The initial conditions for the classical propagation can be obtained from the probability distribution of tunnelling ionization events. Within the adiabatic (quasi-static) tunnelling scenario, the corresponding ionization rate by Ammosov, Delone, and Krainov (ADK) [67]

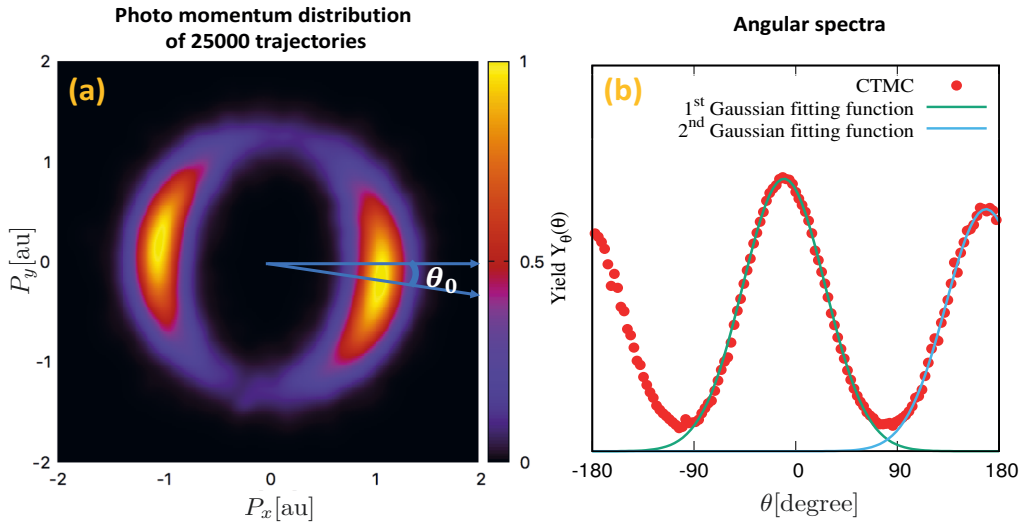

FIGURE 4.3: PMD and the angular spectra of the ionized electrons obtained from CTMC calculations are shown in (a) and (b), respectively. The parameters chosen for this plot are intensity $I = 2 \times 10^{14}$ W/cm^2, wavelength $\lambda = 800$ nm, number of optical cycles $N = 7$, ellipticity $\varepsilon = 0.85$ and ionization potential $I_\mathrm{p} = 0.58$ au for an Ar atom.

is given by

$$R_0(t_0) = C_l^2 \frac{2l+1}{2} \left(\frac{4I_\mathrm{p}}{F(t_0)} \right)^{2/\sqrt{2I_\mathrm{p}}-1} \exp\left(\frac{-2(2I_\mathrm{p})^{3/2}}{3F(t_0)} \right). \tag{4.7}$$

l is the angular-momentum quantum number of the initial bound state of atom, $F(t) = |\vec{F}(t)|$ is the instantaneous field amplitude of the electric field in Eq. (2.6) at the time t. In our simulations, we have taken the values of l and the normalization constant C_l from Ref. [69]. The initial longitudinal momentum is typically assumed to be zero and the probability of the initial transverse momentum $p_{0,\perp}$ is distributed by the function

$$R_1(p_{0,\perp}, t_0) = \frac{(2I_\mathrm{p})^{1/4}}{\sqrt{\pi F(t_0)}} \exp\left(-\frac{\sqrt{(2I_\mathrm{p})} p_{0,\perp}^2}{F(t_0)} \right) \tag{4.8}$$

according to the ADK model (see [68]). Therefore, each trajectory is weighted by

$$R_\mathrm{tot}(p_{0,\perp}, t_0) = R_0(t_0) R_1(p_{0,\perp}, t_0). \tag{4.9}$$

Including the ground state depletion effect (GSD [81, 83], see also the appendix C), each trajectory is weighted by

$$R_{\mathrm{tot,G}}(p_{0,\perp}, t_0) = R_{\mathrm{tot}}(p_{0,\perp}, t_0)\rho(t_0). \tag{4.10}$$

Here, $\rho(t)$ is the survival probability of the ground state, defined by

$$\rho(t) = \exp\left(- \int_{-\infty}^{t} R_0(t')dt' \right). \tag{4.11}$$

For the 2-dimensional problem with an elliptically-polarized field (Eq. (2.6)) with polarization in the xy plane, the initial positions and momenta are given by

$$r_{0,y} = -\frac{F_y(t_0)}{F(t_0)}\, r_e, \qquad p_{0,\perp y} = \frac{F_x(t_0)}{F(t_0)}\, p_{0,\perp p}, \tag{4.12a}$$

$$r_{0,x} = -\frac{F_x(t_0)}{F(t_0)}\, r_e, \qquad p_{0,\perp x} = -\frac{F_y(t_0)}{F(t_0)}\, p_{0,\perp p}. \tag{4.12b}$$

Here, r_e is the tunnelling exit-radius. The transverse momentum $p_{0,\perp}$ can be divided into two components i. e.

$$p_{0,\perp}^2 = p_{0,\perp p}^2 + p_{0,\perp z}^2. \tag{4.13}$$

$p_{0,\perp p}$ is orthogonal to the instantaneous field direction but lies in the plane of polarization, and $p_{0,\perp z}$ is along the z axis which is typically assumed as zero [97].

The final angle depends sensitively on the assumption we make on r_e and $p_{0,\perp p}$. Different existing theoretical assumptions on r_e will be discussed in appendix E. The theory discussed therein is based on adiabatic tunnel ionization, where the electron's energy during tunnelling is conserved and given by the ionization potential I_{p}. In the case of non-adiabatic tunnel ionization, the electron's energy is not conserved and depends on the instantaneous field amplitude resulting in the modification of r_e. Various theoretical models have been proposed in the non-adiabatic regime [41, 72, 84]. In section 4.7, we will propose a new way to determine r_e that is different from the conventional ones. Using the available experimental data our analytical formula is presented in section 4.7. This newly proposed exit radius is consistent with the non-adiabatic results in [41].

4.3.3 PMD and the offset angle

The photo electron-momentum distribution (PMD) (Eq. (4.5)) is calculated here with the CTMC simulation method in this section. For this purpose, 25000 trajectories have been launched while the ionization time t_0 and the transverse momentum $p_{0,\perp p}$ are sampled according to the distribution in Eq. (4.10) in the parameter space $\left[-\frac{NT}{2}, \frac{NT}{2}\right]$ and [-3 σ, 3 σ], respectively. Here, $\sigma = \frac{\sqrt{F(t_0)}}{(2I_\mathrm{p})^{1/4}}$ is the width of the Gaussian probability distribution function for the transverse momentum in Eq. (4.8), and N is the number of optical cycles within a Cos4 envelope, cf. Eq. (2.10). The sampling of the initial conditions has been performed according to the method described in [17]. This method is way more efficient than to propagate a uniform distribution of initial conditions and then to weight the observable by the total tunnelling-ionization probability. The tunnel exit-radius r_e is chosen within the adiabatic tunnelling-ionization scenario with parabolic coordinates ([21],[98]), cf. Eq. (E.4).

After setting up the initial conditions, the trajectories are propagated until the end of the pulse with Hamiltonian equations of motion for the Hamiltonian in Eq. (2.15). Then the asymptotic momentum $\vec{P}$ is calculated for each of the trajectories using Eq. (4.5).

The PMD is shown in figure 4.3 with a laser pulse of wavelength $\lambda = 800$ nm, ellipticity $\varepsilon = 0.85$, $N = 7$ optical cycles, and intensity $I = 2 \times 10^{14}$ W/cm^2 for an Ar atom with ionization potential $I_\mathrm{p} = 0.58$ au. The spectra of the asymptotic momentum is calculated from

$$Y_P = \sum_{i=1}^{n} K_{\delta p}(p_{xi} - P_x)\ K_{\delta p}(p_{yi} - P_y), \tag{4.14}$$

with

$$K_{\delta p}(a) = \frac{1}{\sqrt{\pi}\delta p} \exp\big(-\frac{a^2}{\delta p^2}\big). \tag{4.15}$$

Here, δp is chosen such that the above Kernel K satisfies the following relation

$$\int_{-\infty}^{\infty} da\ K_{\delta p}(a) = 1. \tag{4.16}$$

The summation in Eq. (4.14) has been performed numerically by constructing a 2D grid of dimension $n = 25000$ on the x and y component of the asymptotic momentum P,

which are P_x and P_y respectively. Here, (p_{yi}, p_{xi}) implies the i^{th} point on this grid. The PMD Y_P is plotted as a function of P_x and P_y in Fig. 4.3(a).

Now, to find θ_0, the angular-spectra Y_θ have been calculated with

$$Y_\theta = \sum_{i=1}^{n} K_{\delta\theta}(\eta_i - \theta), \tag{4.17}$$

where $\eta_i = \tan^{-1}\left(\frac{p_{yi}}{p_{xi}}\right)$, and $\theta = \tan^{-1}\left(\frac{P_y}{P_x}\right)$ is the polar angle in the photo electron-momentum plane. The kernel K is given by

$$K_{\delta\theta}(\vartheta) = \frac{1}{\sqrt{\pi}\delta\theta} \exp\big(-\frac{\vartheta^2}{\delta\theta^2}\big). \tag{4.18}$$

Here, $\delta\theta$ is chosen in such a way that K satisfies the relation

$$\int_0^{2\pi} d\vartheta \; K_{\delta\theta}(\vartheta) = 1. \tag{4.19}$$

The angular-spectrum Y_θ in Eq. (4.17) has two maxima, as shown in Fig. 4.3(b). The spectrum is fitted by Gaussian functions near the maxima, yielding the two peak positions at $\theta_1 = -10.32$ and $\theta_2 = 168.46$ degrees. They are almost 180 degrees apart from each other as they correspond to the two maxima of the PMD (Fig. 4.3(a)). Since the laser pulse is finite with a short duration, the two peaks do not lie exactly opposite to each other. If one would use a long pulse, peaks in exact opposition would be achieved. Here, the offset angle θ_0 is calculated as the absolute average of the above two peak-positions, which gives

$$\theta_0 = 10.93^\circ. \tag{4.20}$$

4.4 Analytical formula for the attoclock angle

In the previous chapter, we have seen that the dynamics of an ionized electron in the presence of an external oscillatory laser field becomes much easier to analyse when the laser-atom interaction is described in the Kramers-Henneberger (KH) frame. Using the

KH frame description, we obtain an approximated analytical expression for the attoclock offset angle.

4.4.1 Impulse from the KH potential

In the previous chapter we have seen that when an electron's trajectory is described in a KH potential, there are no wiggles visible, even in the presence of an oscillatory laser field. The Hamiltonian describing the laser-driven dynamics of an electron in the KH frame is given by Eq. (3.1). For the simplest case with CW laser, the initial conditions Eq. (3.9) in the KH frame corresponding to the most-probable trajectory (the ionization probability Eq. (4.7) is highest at the maximum of the field amplitude $F(t_0)$ which occurs at $t_0 = 0$ for the laser pulse defined in Eq. (2.6) and (2.7)) are given by

$$y(t_0 = 0) = r_e + r_\mathrm{q} \qquad p_y(t_0 = 0) = 0 \tag{4.21a}$$

$$x(t_0 = 0) = 0 \qquad p_x(t_0 = 0) = \varepsilon p_\mathrm{q}, \tag{4.21b}$$

where, $p_\mathrm{q} = \omega r_\mathrm{q}$ is the quiver momentum.

The asymptotic momentum can be obtained by the impulse from the KH potential, given by

$$\vec{P} = -\int_{t_0}^{\infty} dt\ \nabla V(\vec{r}(t) - \vec{r}_\mathrm{q}(t)). \tag{4.22}$$

When different approximations are taken into account, the above impulse integral will lead to an analytical expression for $\vec{P}$, as discussed in the next section.

4.4.2 Approximated analytical expression

A perturbation theory approach can be applied to calculate the impulse integral. In this context, the free-particle solutions for the trajectory $\vec{r}(t)$ are obtained from the Hamiltonian without any potential i. e. $H = p^2/2$ and are given by

$$y^{[0]}(t) = r_e + r_\mathrm{q} \qquad x^{[0]}(t) = \varepsilon p_\mathrm{q} t. \tag{4.23}$$

The above trajectory corresponds to the unperturbed free electron Hamiltonian. The first-order asymptotic momentum is then given by the momentum in the unperturbed problem to which an impulse is added from the KH potential evaluated with the unperturbed trajectory. This gives

$$P_y^{[1]} = P_y^{[0]} - \int_0^\infty dt\ d^{[0]}(t)\ [y^{[0]}(t) - y_\mathrm{q}(t)] \tag{4.24a}$$

$$P_x^{[1]} = P_x^{[0]} - \int_0^\infty dt\ d^{[0]}(t)\ [x^{[0]}(t) - x_\mathrm{q}(t)], \tag{4.24b}$$

where

$$d^{[0]}(t) = |\vec{r}^{\,[0]}(t) - \vec{r}_\mathrm{q}(t)|^{-3}. \tag{4.25}$$

[0] always identifies the unperturbed quantity. From Eq. (4.23) we have

$$P_y^{[0]} = 0 \qquad P_x^{[0]} = \varepsilon p_\mathrm{q}. \tag{4.26}$$

Using $P_y^{[0]}$ and $P_x^{[0]}$ from the above equation into Eq. (4.24), one obtains

$$P_y^{[1]} = -\int_0^\infty dt\ d^{[0]}(t)\ [y^{[0]}(t) - y_\mathrm{q}(t)] \tag{4.27a}$$

$$P_x^{[1]} = \varepsilon p_\mathrm{q} - \int_0^\infty dt\ d^{[0]}(t)\ [x^{[0]}(t) - x_\mathrm{q}(t)]. \tag{4.27b}$$

The above impulse integral has no analytical closed-form solution, it can only be solved numerically. As such there is no advantage compared to Eq. (4.22). However, it is possible to approximate it. To get approximated analytical expressions of this impulse, one should consider that $r_e \gg r_\mathrm{q}$ for low-intensity, referred to as *Case A* below, and, $r_e \ll r_\mathrm{q}$ for high-intensity, referred to as *Case B* in the following.

Case A (low-intensity): For low intensities I, the quiver amplitude r_q is small. We assume that $r_\mathrm{q} \approx 0$ in the integral Eq. (4.27), allowing the following closed-form analytical

expressions for the asymptotic momenta

$$\begin{aligned} P_y^{[1A]} &= -\int_0^\infty dt \frac{y^{[0]}(t)}{\left[[y^{[0]}(t)]^2 + [x^{[0]}(t)]^2\right]^{3/2}} \\ &= -\int_0^\infty dt \frac{[r_e + r_\mathrm{q}]}{\left[[r_e + r_\mathrm{q}]^2 + [\varepsilon p_\mathrm{q} t]^2\right]^{3/2}} \\ &= -\frac{1}{[r_e + r_\mathrm{q}]\varepsilon p_\mathrm{q}}, \end{aligned} \tag{4.28}$$

$$\begin{aligned} P_x^{[1A]} &= \varepsilon p_\mathrm{q} - \int_0^\infty dt \frac{x^{[0]}(t)}{\left[[y^{[0]}(t)]^2 + [x^{[0]}(t)]^2\right]^{3/2}} \\ &= \varepsilon p_\mathrm{q} - \int_0^\infty dt \frac{[\varepsilon p_\mathrm{q} t]}{\left[[r_e + r_\mathrm{q}]^2 + [\varepsilon p_\mathrm{q} t]^2\right]^{3/2}} \\ &= \varepsilon p_\mathrm{q} - \frac{1}{[r_e + r_\mathrm{q}]\varepsilon p_\mathrm{q}}, \end{aligned} \tag{4.29}$$

here $y^{[0]}(t)$ and $x^{[0]}(t)$ are used from Eq. (4.23). Surprisingly, the above two integrals give the same results, and the final momentum differs by the initial momentum only. The corresponding asymptotic angle in the momentum plane is obtained as the absolute of arctangent of the ratio between the y-component and x-component momentum.

$$\theta_{0A} = \left| \tan^{-1}\left(\frac{P_y^{[1A]}}{P_x^{[1A]}}\right) \right|. \tag{4.30}$$

The dependence of the laser parameters within these equations are discussed below.

$P_y^{[1A]}$ decreases with quiver amplitude r_q, and the initial momentum εp_q. This makes it decrease as a function of field amplitude. The explicit dependence on the field amplitude with $r_e = r_{e,\,\mathrm{SFA}}$, cf. Eq. (E.3) can be seen from

$$P_y^{[1A]} = -\frac{\omega}{\varepsilon(I_\mathrm{p} + F_\varepsilon^2/\omega^2)}. \tag{4.31}$$

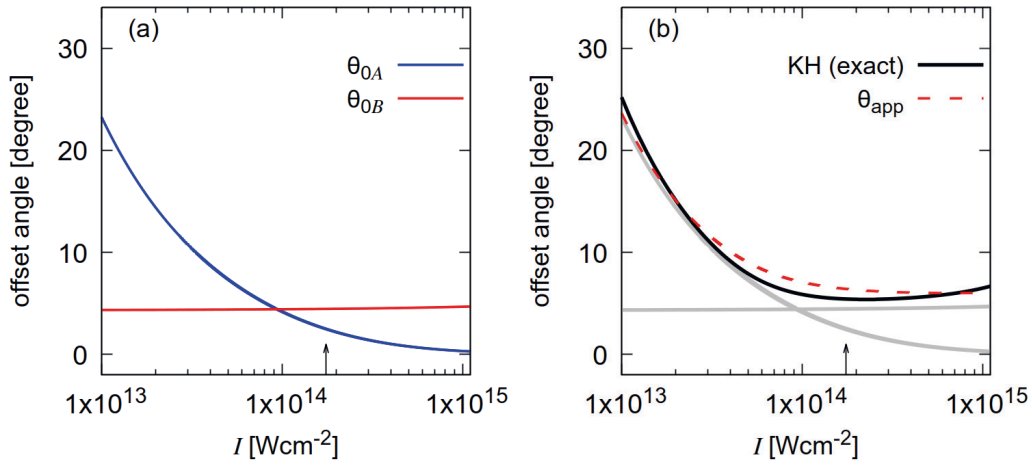

FIGURE 4.4: (a) : The intensity dependence of the analytical offset angle for the low-intensity branch θ_{0A} in Eq. (4.30) (blue solid curve) and for the high-intensity-branch θ_{0B} in Eq. (4.37) (red solid curve). (b) : Intensity dependence of the analytical angle $\theta_{\rm app}$ in Eq. (4.41) (red dashed curve) and the real offset angle as obtained in a KH problem in Eq. (3.1) (black solid curve). The curves from (a) are represented by gray solid lines. Intensity is given by $I = F^2_{\rm max}$. Here $N = 2$ optical-cycles, wavelength $\lambda = 800$ nm, ellipticity $\varepsilon = 1.0$, and $I_{\rm p} = 0.9$ au for the He atom.

$P_x^{[1A]}$ increases with the initial momentum, hence also with the field amplitude, as seen from

$$P_x^{[1A]} = \varepsilon F_\varepsilon/\omega. \tag{4.32}$$

This results in the angle to follow the same qualitative behaviour as $P_y^{[1A]}$ does as a function of field amplitude, which is explicitly simplified in

$$\theta_{0A} = \left| \tan^{-1}\left(\frac{\omega^2}{\varepsilon^2 F_\varepsilon (I_{\rm p} + F_\varepsilon^2/\omega^2)} \right) \right|. \tag{4.33}$$

From this equation it is clear that the angle decreases with the field amplitude viz. intensity I (see Fig. 4.4(a) (blue solid curve)).

Clearly, two terms compete with each other. These are the electron's kinetic energy (KE) and potential energy (PE) due to the Coulomb attraction with the parent ion at the release time. When I increases, the initial momentum increases, and r_e decreases, increasing both the KE and PE. However, both of these energies have a different impact on the final angle. The higher KE causes a smaller angle. On the contrary, higher PE

causes a larger angle. Therefore, whether the angle decreases or increases as a function of I is decided by the dominants of KE or PE. Within the present low-intensity regime, the KE dominates over the PE because of the larger r_e. So, the angle decreases with increasing I.

However, above some critical intensity where the quiver amplitude r_q becomes comparable with the tunnel exit-radius r_e, such low-intensity approximation remains no longer valid. The critical intensity I_* is reached at $r_\mathrm{q} = r_e$, and for the SFA barrier exit Eq. (E.3) it can be calculated as

$$\begin{aligned} \frac{F_{\varepsilon *}}{\omega^2} &= \frac{I_\mathrm{p}}{F_{\varepsilon *}} \\ \text{or, } F_* &= \omega\sqrt{I_\mathrm{p}(1+\varepsilon^2)}, \end{aligned} \tag{4.34}$$

for a circularly-polarized laser pulse ($\varepsilon = 1$) of wavelength 800 nm, the critical intensity $I_* = F_*^2$ for a Helium atom with $I_\mathrm{p} = 0.9$ au equals 1.75×10^{14} W/cm^2 (as marked by '↑' in Fig. 4.4). Next we investigate the impulse integral in Eq. (4.27) for high-intensity i. e. $I \gtrsim I_*$, and discuss the approximations required to obtain an analytical expression of the attoclock angle in this regime.

Case B (high-intensity): For $r_\mathrm{q} \gtrsim r_e$, we cannot neglect the terms containing r_q as we did for low intensity. Due to the high intensity, the initial momentum $p_0 = \varepsilon\omega r_\mathrm{q}$ (Eq. (4.21)) of the electron becomes large, and therefore the ionized electron flies very quickly away from the parent-ion with a large momentum. From Fig. 4.5, we see that the y-component of the KH force $F_y(= \dot{p}_y)$ (the major-axis of the polarization-ellipse) obtained from the Hamilton's equations of motion corresponding to the KH Hamiltonian in Eq. (3.1) decreases faster to zero at high intensities within a very short timescale ($t/T \ll 1 \Rightarrow \omega t \ll 1$) after the electron reaches the barrier at $t = 0$. Therefore, we can Taylor-expand the sinusoidal-terms in Eq. (4.27) up to second-order in t, i. e., $\sin(\omega t) \approx \omega t$, $\cos(\omega t) \approx 1 - \omega^2 t^2/2$ (Within such approximations, the elliptical motion of the KH potential as depicted in Fig. 3.1 is approximated as a hyperbolic motion and the corresponding KH trajectory can be described by an accelerated Kepler problem (AKP) [99],[100], see appendix D). Thus in the high-intensity regime, as the electron is released from the parent-ion within a very short time, its asymptotic momenta can be

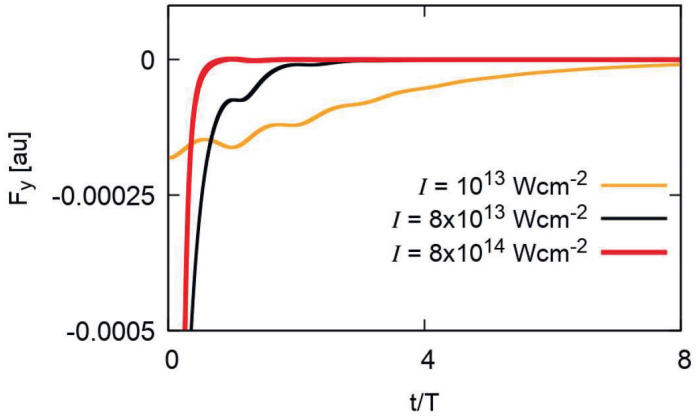

FIGURE 4.5: The component along the y-axis (the major-axis of the polarization-ellipse) of the KH force F_y as function of t. The parameters are $N = 4$ optical-cycles, wavelength $\lambda = 800$ nm, ellipticity $\varepsilon = 1.0$, and $I_\mathrm{p} = 0.9$ au for the He atom.

approximated in the following simplified form with the analytical expression

$$\begin{aligned} P_y^{[1B]} &= -\int_0^\infty dt \frac{y^{[0]}(t) - r_\mathrm{q}[1-\omega^2 t^2/2]}{\left[\left[y^{[0]}(t) - r_\mathrm{q}[1-\omega^2 t^2/2]\right]^2 + \left[x^{[0]}(t) - \varepsilon\omega r_\mathrm{q} t\right]^2\right]^{3/2}} \\ &= -\int_0^\infty dt \frac{1}{[r_e + \frac{1}{2} r_\mathrm{q}\omega^2 t^2]^2} \\ &= -\frac{\pi}{\sqrt{F_\varepsilon [2r_e]^3}}, \end{aligned} \tag{4.35}$$

$$\begin{aligned} P_x^{[1B]} &= \varepsilon p_\mathrm{q} - \int_0^\infty dt \frac{x^{[0]}(t) - \varepsilon\omega r_\mathrm{q} t}{\left[\left[y^{[0]}(t) - r_\mathrm{q}[1-\omega^2 t^2/2]\right]^2 + \left[x^{[0]}(t) - \varepsilon\omega r_\mathrm{q} t\right]^2\right]^{3/2}} \\ &= \varepsilon p_\mathrm{q}, \end{aligned} \tag{4.36}$$

where $y^{[0]}(t)$, $x^{[0]}(t)$ are from Eq. (4.23). The integral in $P_x^{[1B]}$ is zero because the numerator of the integrand becomes zero which certainly follows from Eq. (4.23). The corresponding asymptotic angle in the momentum plane is

$$\theta_{0B} = \left| \tan^{-1}\left(\frac{P_y^{[1B]}}{P_x^{[1B]}}\right)\right|. \tag{4.37}$$

$P_y^{[1B]}$ shows a different qualitative behaviour as a function of intensity than $P_y^{[1A]}$. By using the SFA formula for r_e, cf. Eq. (E.3), $P_y^{[1B]}$ is reduced to

$$P_y^{[1B]} = -\frac{\pi F_\varepsilon}{\sqrt{(2I_\mathrm{p})^3}}, \tag{4.38}$$

therefore it is linearly proportional to the field-amplitude. $P_x^{[1B]}$ is also linearly proportional to the field amplitude, resulting in no intensity dependence on the final angle. The momentum along the major axis of the polarization ellipse has also been obtained within the CCSFA approach [15, 18, 20, 39, 101].

The final angle of Eq. (4.37) is plotted in Fig. 4.4(a) (red solid curve), for $r_e = r_\mathrm{Para}$, cf. Eq. (E.4). One can see the weak dependence of the angle on I for this high-intensity branch. It is understood that there are two facts responsible for the feature of the final angle as a function of I, which are the KE, and the PE, respectively, and both of them have opposite effects. In this intensity regime, they almost balance each other, resulting in the weak dependence of θ_{0B} on I.

This high-intensity approximation relies on the fact that the electrons fly away from the parent-ion with a high initial momentum. Since the initial momentum follows the relation $p_0 = \varepsilon F_\varepsilon/\omega$ (Eq. 4.21), i. e., it increases with ellipticity but decreases with frequency, the approximation becomes more valid for the laser pulse with higher ellipticity but lower frequency as discussed later in section 4.6.2.

We connect the above described two extreme cases by adapting the avoided crossing method of a two-level system where we consider θ_{0A} and θ_{0B}, cf. Eq. (4.30) and (4.37) respectively, as the two levels, leading us to construct the following matrix with a real matching-factor δ,

$$\Theta = \begin{bmatrix} \theta_{0A} & 0 \\ 0 & \theta_{0B} \end{bmatrix} + \begin{bmatrix} 0 & \delta \\ \delta & 0 \end{bmatrix}. \tag{4.39}$$

The two eigenvalues of Θ are given by

$$\theta_\pm = \frac{(\theta_{0A} + \theta_{0B})}{2} \pm \sqrt{\frac{(\theta_{0A} - \theta_{0B})^2}{4} + \delta^2}, \tag{4.40}$$

out of which we choose θ_+ as the analytical angle since asymptotically it approaches to θ_{0A} and θ_{0B}, and therefore the approximated offset angle is given by

$$\theta_{\text{app}} = \frac{(\theta_{0A} + \theta_{0B})}{2} + \sqrt{\frac{(\theta_{0A} - \theta_{0B})^2}{4} + \delta^2}. \tag{4.41}$$

The matching factor is calculated as follows. From Eqs. (4.31) and (4.38), we can see that P_y, for the low-intensity branch, decreases with intensity and for the high-intensity branch, increases with intensity i. e. P_y behaves qualitatively the same as the angle. Therefore, the P_y from these two intensity branches, are connected as

$$P_{y,\text{app}} = \frac{(P_y^{[1A]} + P_y^{[1B]})}{2} + \sqrt{\frac{\left(P_y^{[1A]} - P_y^{[1B]}\right)^2}{4} + \delta^2}, \tag{4.42}$$

where

$$P_y^{[1A]} = -\frac{\omega}{(I_\text{p} + F_\varepsilon^2/\omega^2)}, \text{and} \quad P_y^{[1B]} = -\frac{\pi F_\varepsilon}{\sqrt{(2I_\text{p})^3}}. \tag{4.43}$$

For the attoclock setup, ellipticities lie in the range $0.8 < \varepsilon < 1$, therefore, here, to obtain $P_y^{[1A]}$, we have used $\omega/\varepsilon \to \omega$ in Eq. (4.31). This two momenta $P_y^{[1A]}$ and $P_y^{[1B]}$, as a function of F_ε, cross each other ($P_y^{[1A]}$ decreases with F_ε, and $P_y^{[1B]}$ increases with F_ε), and from our previous discussion, we know that the crossing occurs approximately at $F_\varepsilon = F_{\varepsilon*}$, cf. Eq. (4.34). At this point, we use the observation that the actual offset angle has a minimum near the crossing, therefore near $F_\varepsilon = F_{\varepsilon*}$, which is also true for the total momentum $P_{y,\text{app}}$. Hence, to obtain the value of δ, we solve the following equation

$$\frac{dP_{y,\text{app}}}{dF_\varepsilon} = 0, \tag{4.44}$$

at $F_\varepsilon = F_{\varepsilon*} = \omega\sqrt{I_\text{p}}$. It is just an approximation based on observation. At the actual crossing point δ equals zero, however, since the crossing is not exactly at $F_{\varepsilon*}$, this equation gives a measure of the finite delta as a function of frequency ω, and ionization potential I_p,

$$\delta(\omega, I_\text{p}) = \frac{3\omega}{4I_\text{p}}. \tag{4.45}$$

This qualitative behaviour of $\delta(\omega, I_\text{p})$ is understood as follows. For the atoms with lower I_p, the electron experiences a stronger Coulomb attraction force at the tunnel exit because

it is closer to the parent ion (r_e is small); this can also be seen from Eqs. (E.2)-(E.4). This high Coulomb attraction prevents the electron from flying away quickly from the parent-ion because of low initial KE, and hence the short-time Taylor-expansions that have been used to obtain Eq. (4.37) are not valid. This deviation for lower I_p can be compensated by tuning δ, and therefore as lower the I_p is larger is the δ. The ω-dependence of δ is also explained by a similar logic, i. e., as larger the ω is, as lower is the initial momentum/KE. The high-intensity approximation is accordingly less valid, requiring larger compensation through δ. Therefore the proportionality with the frequency ω in $\delta(\omega, I_\mathrm{p})$ is justified.

In Fig. 4.4(b), θ_app from Eq. (4.41) is plotted (red dashed curve) as a function of intensity I which agrees very well with the exact angle (black solid curve) obtained from the KH problem. In the subsequent sections we will discuss how well this analytical formula behaves as compared to other theories, and agrees with the numerical simulations and available experimental results.

4.5 Other theoretical studies of the offset angle

A conclusive picture is shown in Fig. 4.6, where we compare our results with other established works, which are briefly discussed below.

According to the Keldysh-Rutherford (KR) model, the final attoclock offset angle can be obtained from a Rutherford scattering problem [102], which yields

$$\theta_0 = \frac{\omega^2}{I_\mathrm{p}} \frac{1.0 + \alpha}{I^{0.5+\beta}}. \tag{4.46}$$

However, this is valid only for the CP pulse with ellipticity $\varepsilon = 1.0$. Moreover, we see from Fig. 4.6 that it satisfies the numerically obtained angle for very low intensities and deviates when the intensity is high. Another approach, namely Coulomb corrected SFA (CCSFA), was first introduced by Goreslavski *et al* [15]. The final photo-electron momentum is corrected as an impulse from the Coulomb potential. The trajectory required for calculating such an impulse is obtained using the SFA. Considering this theory, the

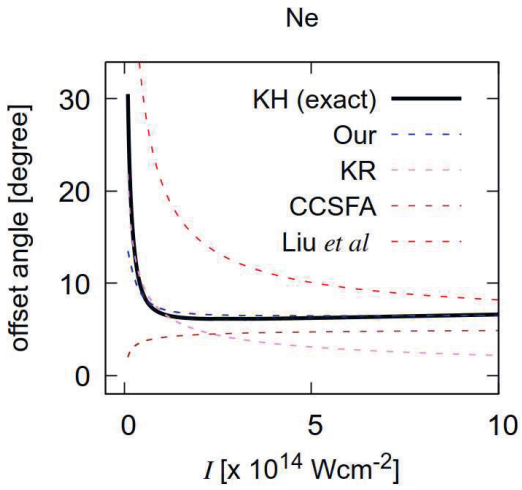

FIGURE 4.6: Final offset angle as a function of intensity for different models. see the text for details.

offset angle is given by

$$\theta_0 = \tan^{-1}\left(\frac{\pi}{(2r_e)^3 F(t_0) A(t_0)}\right) \tag{4.47}$$

$F(t_0)$ and $A(t_0)$ respectively are the amplitude of the electric-field and vector potential at the ionization time. Although θ_0 in Eq. (4.47) agrees with the numerically obtained values for the higher intensity, a noticeable deviation can be seen from Fig. 4.6 for the low intensities. Last but not least, Liu *et al* provided the following expression of the offset angle for a CP pulse [83]

$$\theta_0 = \tan^{-1}\left(\frac{1}{R-1}\right), \tag{4.48}$$

where $R = F_{\max}/(2\omega p_c)$ with p_c being the difference in the final momentum and the corresponding SFA momentum along the minor axis of the polarization ellipse.

The offset angle variation with intensity obtained using the above theoretical models is compared and summarized in Fig. 4.6 for a Ne atom. It can be clearly seen that our predicted analytical angle provides the best agreement with the exact numerical result compared to the existing theories.

4.6 Connections with the CTMC results

In the following we obtain the attoclock offset angle (θ_0) by performing CTMC simulations, as discussed in section 4.3 and compare them with the analytical prediction for the angle in Eq. (4.41) for different atomic ionization potentials and laser parameters.

4.6.1 Different ionization potentials

To study the intensity dependence of the attoclock angle for different atoms with different ionization potentials I_p, the offset angles from the CTMC simulation are compared with the corresponding analytical prediction. CTMC calculations are done with a CP laser pulse of wavelength $\lambda = 800$ nm and a duration of $N = 2$ optical cycles for four different atoms He, Ne, Ar, H with the ionization potentials listed in Table 4.1. Here, the exit-radius r_e is chosen from the parabolic barrier, cf. Eq. (E.4) because alternatively such as the FDM Model, cf. Eq. (E.2), reads OBI at much lower intensities, as discussed in the appendix E, especially for atoms with lower I_p.

Surprisingly, the results obtained from the CTMC calculations, without ground-state depletion, i. e., setting $\rho(t_0) = 1$ in Eq. (4.10), are in good agreement with the analytically predicted angle as shown in Fig. 4.7. The final angle increases with lowering I_p because lower I_p implies larger Coulomb attraction energy at the exit, resulting in larger final offset angles. This qualitative behaviour is captured by the analytical angle, decreasing with increasing I_p. This can be understood by looking at the momentum $P_{y,\mathrm{app}}$ from Eq. (4.42), where it can be clearly seen that $P_{y,\mathrm{app}}$ increases with decreasing I_p, as does the $P_y^{[1A]}$, $P_y^{[1B]}$, and δ (cf. Eq. (4.45)). Since $P_x \approx \varepsilon\omega r_\mathrm{q}$ does not depend on I_p, the offset angle increases with decreasing I_p. Not only qualitative but reasonable quantitative agreement with the CTMC results are also achieved.

Species	He	Ne	Ar	H
I_p [au]	0.9	0.79	0.58	0.5

TABLE 4.1: Values of ionization potentials I_p for different atomic species.

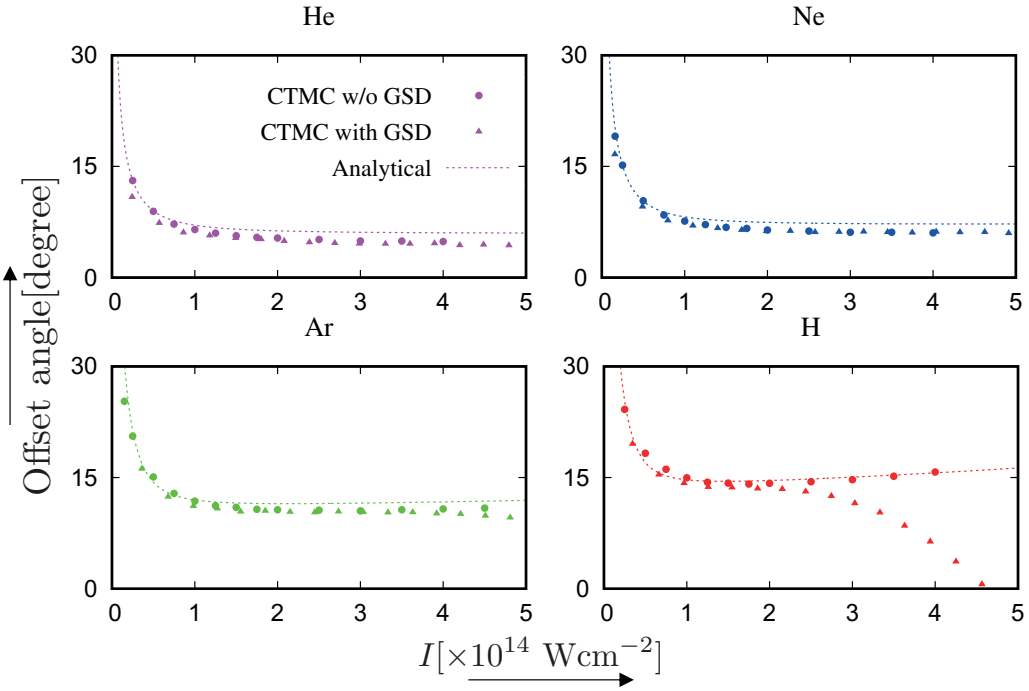

FIGURE 4.7: Offset angle as a function of intensity I for different atoms. Triangles and circles are the CTMC results with and without the ground state depletion (Eq. (4.10)) respectively, performed using the circularly-polarized pulse with $N = 2$, wavelength $\lambda = 800$ nm. The dashed lines are the analytical angle obtained from Eq. (4.41) using parabolic exit-radius (Eq. (E.4)), within the CTMC calculations as well we have considered $r_e = r_{e,\text{Para}}$.

4.6.2 Different laser parameters

To access the validity of the analytical attoclock angle further, we study its ellipticity and frequency dependence for three different atoms (He, Ar, and Kr) and compare them with the offset angle obtained from CTMC calculations, as shown in Fig. 4.8.

We can see from Fig. 4.8(a) that the analytical angle agrees very well with the CTMC-angle for the nearly circularly-polarized laser pulses ($0.8<\varepsilon<1.0$) as a function of ellipticity for all three atoms. Only a small deviation is consistently observed for the lower ellipticities particularly for the atoms with a lower I_p (Ar and Kr), which originates from the low initial momentum for lower ellipticities. This renders the high-intensity approximation less valid, as also discussed before. The offset angle shows a slow decrease as a function of ellipticity for the three atoms, and this behaviour is captured both, in the CTMC results

and the analytical prediction. The increase in ellipticity implies a smaller the field amplitude at the exit, which makes the exit-radius larger. Therefore, the Coulomb attraction of the electron at the release-time decreases, causing a reduction in the final offset angle.

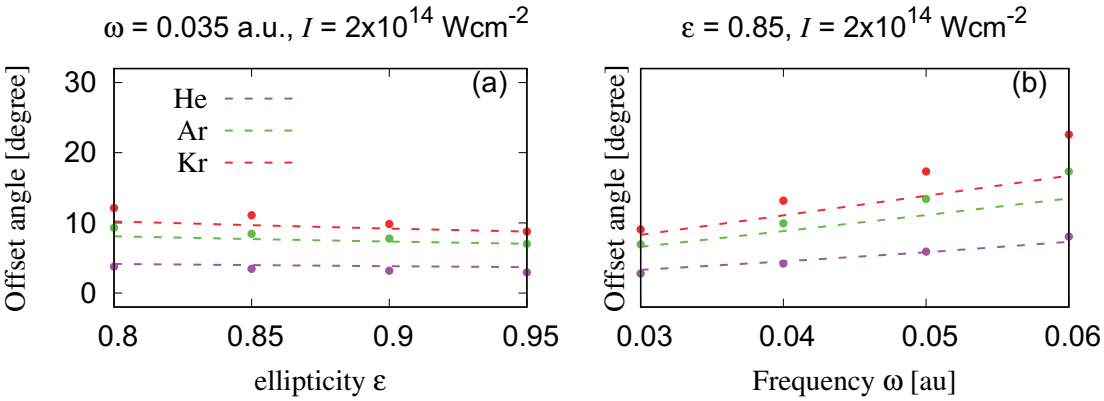

FIGURE 4.8: Offset angle as a function of ellipticity ε (a), and frequency ω (b) for three atoms He, Ar and Kr with the other fixed laser parameters as mentioned at the top of each figure. The points are obtained from CTMC simulation and the dashed lines represent the analytical angle. Number of laser optical cycles used is $N = 3$.

On the other hand, the offset angle increases with frequency ω for both, the CTMC results and the analytical prediction. This occurs because of the lower initial momentum (F_ε/ω, cf. Eq. (4.21)) of the ionized electron at the release-time at higher frequencies, which keeps the escaping electron longer exposed to significant Coulomb attraction, resulting in a higher offset angle. However, as a function of frequency, the analytical prediction deviates from the CTMC results for the higher frequency regime, whereas it agrees reasonably well for the low-frequency laser pulses (see Fig. 4.8(b)). This behaviour is the same for all three atoms. We can identify the reasons for this deviation in the high-frequency regime: firstly, the Taylor expansion used in the derivation of the analytical expression for the angle is valid for $\omega t \ll 1$, which is not fulfilled when ω is high, secondly, the ionized electron's lower initial momentum due to the higher frequency ω renders the high-intensity approximation in the analytical approximation of the angle less valid, which has been also discussed before.

The discussed deviations of the analytical prediction from the CTMC results appear for Ar, and Kr. For He, however, the analytically derived angle is always in good agreement with the CTMC simulations due to the high ionization potential I_p.

4.7 New exit-radius relating to the experiment

In this section, we will propose to define new tunnel exit conditions using the analytical angle and the available experimental data. To this end, the analytical angle is re-written as

$$\theta_\mathrm{exp} = \frac{\theta_{0A}(r_e,\varepsilon,F_\mathrm{max},\omega)+\theta_{0B}(r_e,\varepsilon,F_\mathrm{max},\omega)}{2} + \sqrt{\frac{(\theta_{0A}(r_e,\varepsilon,F_\mathrm{max},\omega)-\theta_{0B}(r_e,\varepsilon,F_\mathrm{max},\omega))^2}{4}+\delta(\omega,I_\mathrm{p})}. \quad (4.49)$$

Here, θ_app from Eq. (4.41) is replaced by θ_exp, which is the attoclock offset angle obtained from the experiment. The formula for θ_{0A}, and θ_{0B}, are used, respectively, from Eq. (4.30), and Eq. (4.37), as a function of $r_e, \varepsilon, F_\mathrm{max}$, and ω, whereas δ is used from Eq. (4.45) as a function of ω, and I_p. Knowing the corresponding laser parameters and I_p of the atoms from the respective experiment, the equation (4.49) is solved for the only unknown r_e by a root-finding method. The solutions (denoted by $r_{e,\mathrm{ext}}$) are plotted as a function of F_max in Fig. 4.9.

Figure 4.9(b) and (c) show the $r_{e,\mathrm{ext}}$ for the Ar and He atom, respectively, with the experimental data taken from A. N. Pfeiffer *et al* [21] which uses an elliptically-polarized laser pulse with ellipticity $\varepsilon = 0.78$, wavelength $\lambda = 740$ nm and 7 fs duration. There are no experimental data available for the absolute offset angle of Kr atoms, but the angle difference between Ar and Kr is provided by N. Camus *et al* [23] for the gas mixture of Ar and Kr. This result is used here to extract the absolute angle for Kr by using the data for Ar atom from [21] as a reference as shown in Fig. 4.9 (a). The experiment on the gas mixture of Ar and Kr uses a laser pulse with ellipticity $\varepsilon = 0.85$, wavelength $\lambda = 1300$ nm and 35 fs duration.

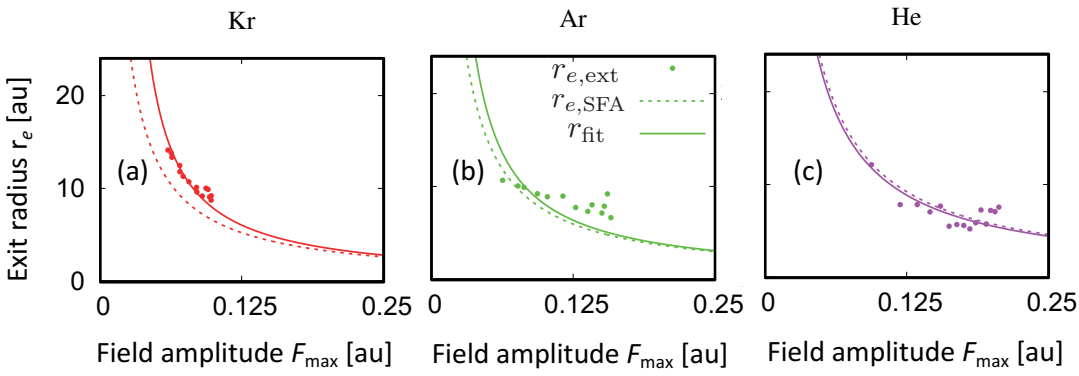

FIGURE 4.9: Tunnel exit-radius r_e as a function of the field amplitude F_{max}. Circles represent r_e extracted from the experiment as described in the text and the dashed lines are the corresponding adiabatic SFA exit barrier (Eq. (E.3)). The solid lines are obtained from the fitting function $r_{\mathrm{fit}} = \frac{(I_{\mathrm{p}}-a)\sqrt{1+\varepsilon^2}}{F_{\mathrm{max}}-F_{\mathrm{s}}}$. The values of the fitting parameters a and F_{s} are listed in Table 4.2.

As described earlier, the exit-radius r_e can not be directly measured in experiment. However, it can be predicted by different theoretical models, as discussed in appendix E, with different implications. Let us now see how the extracted $r_{e,\mathrm{ext}}$ agrees and/or differs from the conventional models. $r_{e,\mathrm{ext}}$ is plotted (filled circles) in Fig. 4.9. As a reference, r_e from the SFA model (dashed lines) cf. Eq. (E.3) is also shown. Although $r_{e,\mathrm{SFA}}$ agrees with the $r_{e,\mathrm{ext}}$ for He atom as shown in Fig. 4.9, this is not true for Ar and Kr. Therefore, we introduce the fitting function

$$r_{\mathrm{fit}} = \frac{(I_{\mathrm{p}} - a)\sqrt{1+\varepsilon^2}}{F_{\mathrm{max}} - F_{\mathrm{s}}}. \tag{4.50}$$

This is a new and unconventional exit-radius that differs from the $r_{e,\mathrm{SFA}}$ in the numerator by subtracting a fitting parameter a from I_{p}, and in the denominator where the F_{max} is subtracted by a second fitting parameter F_{s}. The parameter a acknowledges non-adiabatic tunnelling ionization which changes the energy at the tunnel exit with respect to I_{p}. With F_{s} we take into account that ionization can happen before F_{max} is reached. The fitted values of a and F_{s}, are listed in Table 4.2 corresponding to Fig. 4.9(a), (b), (c), respectively, for Kr, Ar, and He atoms. The new exit-radius (solid lines) agrees reasonably well with the extracted exit-radius r_{ext} from the experiment. The physics behind the monotonic behaviour (shown in Table 4.2) of a and F_{s} with I_{p} is discussed below.

species	I_p[au]	a[au]	F_s[au]
Kr	0.51	0.0	0.017
Ar	0.58	0.0	0.008
He	0.9	0.04	0.0

TABLE 4.2: a, F_s values in r_{fit} in Eq. (4.50).

It can be seen from Table 4.2 that the $a \neq 0$ for the He atom. This results from the non-adiabatic tunnel ionization. The electrons reach the tunnel-exit with lower total energy than the quasi-static energy I_p because the electron gains energy on the way to the tunnel-exit due to the time-dependent electric field. It should be noted that this non-zero value of a can be compared with the corresponding non-adiabatic energy as calculated by the classical back-propagation method for the He atom obtained in [41]. The energy therein lies on an average 0.1 au above $-I_p$. The fitted value for us is 0.04 au (Table 4.2). Note that a is zero for atoms with lower I_p. In the present high-intensity regime, for those lower I_p, the barrier-width is so small that the electron reaches the exit too fast to gain energy.

On the other hand, F_s is zero for He and monotonically increases going from high I_p (Ar) to low I_p (Kr). This comes from the early ionization events occurring due to ground state depletion, as discussed in appendix C. So far, in the analytical derivation of the offset angle (Eq. (4.41)), we have not considered the ground state depletion, and therefore we set $\rho(t_0) = 1$ in Eq. (4.10). This implies that the ionization probability is highest at the field-maximum, which occurs at $t_0 = 0$ (Eqs. (2.6)-(2.7) and (4.7)). However, considering the ground state depletion i. e. $\rho(t_0) \neq 1$ (cf. Eq. (4.11)), the highest ionization probability occurs earlier than the field's peak at $t_0<0$. Therefore, this early ionization effect is taken care by subtracting a positive shift F_s from the field-maximum F_{max} in r_{fit}. Since the ground state depletion effect increases with lowering I_p (see appendix C), the shift F_s also increases.

4.8 Analytical shift for the bicircular attoclock

To get more insight from our theory, we apply it in this section, for an attoclock setup with bicircularly-polarized laser pulses [103]. The vector potential of the bicircular field

is given by

$$\vec{A}(t) = -\frac{F_{\max}/\omega}{\sqrt{1+\varepsilon^2}}\left(\begin{bmatrix}\cos(\omega t)\\ \sin(\omega t)\end{bmatrix} + \varepsilon/2\begin{bmatrix}\pm\cos(2\omega t)\\ \sin(2\omega t)\end{bmatrix}\right), \tag{4.51}$$

where a plus, and a minus sign represents a co-rotating and a counter rotating bi-circular pulse, respectively.

Now, considering the low-intensity approximation ($r_{\rm q} \approx 0$, *Case A*) and the high-intensity approximation (Taylor-expansion of all the sinusoidal terms upto second order in time t, *Case B*) within the impulse from the KH potential, cf. Eq. (4.22), with the co-rotating bi-circular laser field, the asymptotic momentum P_y assumes the form

$$P_y^{[1A]} = -\frac{\omega^3}{[I_{\rm p}\omega^2(1+\varepsilon) + F_\varepsilon^2(1+\varepsilon/4)](1-\varepsilon/2)} \tag{4.52a}$$

$$P_y^{[1B]} = -\frac{\pi F_\varepsilon(1+\varepsilon)}{\sqrt{(2I_{\rm p})^3}}. \tag{4.52b}$$

It is clear from the above equations that $P_y^{[1A]}$ and $P_y^{[1B]}$, respectively, fall and increase with the field-amplitude F_ε. They cross near $r_e = r_{\rm q}$, which correspond to the critical field-amplitude

$$F_{\varepsilon *} = \frac{\omega\sqrt{I_{\rm p}}}{(1+\varepsilon)\,(1+\varepsilon/4)}. \tag{4.53}$$

Using the same process as adopted for the CP pulses, the two branches are connected by the matching factor δ, which is determined here for the bicircular pulse with $\varepsilon = 1/2$ as a function of ω, and $I_{\rm p}$ to be

$$\delta = \frac{0.51\omega}{I_{\rm p}}. \tag{4.54}$$

The final momentum is calculated as

$$P_{y,\rm app} = \frac{(P_y^{[1A]} + P_y^{[1B]})}{2} + \sqrt{\frac{\left(P_y^{[1A]} - P_y^{[1B]}\right)^2}{4} + \delta^2}, \tag{4.55}$$

where $P_y^{[1A]}$, $P_y^{[1B]}$, and δ are obtained from Eqs. (4.52)(a)-(b), and (4.54), respectively.

For $\varepsilon = 1/2$, the respective field is known as quasi-linear field as described in [103], and for the laser parameters used in that article, i. e., intensity $I = 7 \times 10^{14}$ Wcm^{-2} and

wavelength $\lambda = 800$ nm for He atom, the momentum in Eq. (4.55) gives

$$P_{y,\mathrm{app}} = 0.1878 \text{ au.} \tag{4.56}$$

This agrees well with the shift in momentum P_y in Fig. 1(c) of [103], which is around 0.2 au.

4.9 Summary

Attoclock or attosecond angular streaking is a powerful technique to probe the microscopic dynamics of tunnel-ionized electrons by an intense, elliptically-polarized laser pulses. The asymptotic angle with which the ionized electrons reach the detector is measured in the two-dimensional photo electron-momentum plane. In this chapter we have studied such microscopic dynamics of electrons classically. In this context, we have derived an analytical expression for the attoclock angle corresponding to the most-probable electron trajectory. The derivation is based on the impulse approximated from the Kramers-Henneberger potential; the separation of the impulse integral into the low-intensity (exit-radius is much larger than the quiver amplitude) and high-intensity (quiver amplitude is much larger than the exit-radius) allowed us to obtain an approximate analytical formula in these two intensity regimes, separately, which is then combined by introducing a matching-factor δ using the concept of avoided-crossings of two-state systems, which determines the continuation from the two intensity regimes for each intensity.

Surprisingly, the analytical formula agrees very well with the one obtained from the classical-trajectory Monte Carlo (CTMC) simulations for atoms with high I_p and nearly circularly-polarized, low-frequency laser pulses for a large range of laser intensities. Moreover, this formula shows both, qualitative and quantitative agreement with the CTMC results with various models for the tunnel exit-radius r_e.

Furthermore, we have verified the validity of the analytical angle by comparing with the available experimental data for He, Ar, and Kr atoms. In particular, we have proposed an unconventional and experimentally relevant exit-radius r_e. The tunneling exit-radius

enters our approximate determination of the attoclock angle and can therefore be determined experimentally within our approach through measured attoclock angles. On the other hand, we can fit the exit-radius obtained in this way to properties of the laser pulse and the target atom (I_p) only, which provides reasonable insight, consistent with the tunnelling ionization scenario. The simulation can be further extended to quantum mechanical ones to check the validity and consistency of this proposed exit criteria.

Chapter 5

Summary and conclusions

This thesis has investigated the post-tunnelling ionization dynamics of electrons in the presence of intense laser-atom interaction classically. An elliptically-polarized laser pulse polarized in a two-dimensional plane has been considered throughout the work, which allows the electron to reach the detector without any re-scattering. We studied the dynamics of such 'direct electrons' and focussed particularly on two problems in this thesis.

Chapter 3 finds that the ionized electron dynamics can be governed by an emergent static ring potential, albeit an oscillatory laser is present. The ring potential has been formed by making a short-time Taylor-series expansion of the time-dependent Kramers Henneberger (KH) potential, which describes the dynamics exactly. The validity of the theory relies on the large initial momentum of the electron, which drives it quickly away from the moving KH potential. The time-dependent motion thereby only affects the dynamics immediately after its release from the parent-ion, but it does not have impact when the electron is far away. Therefore, the short-time expansion holds, and this leads to the formation of a static potential. Practically, such a large momentum can be gained with larger ellipticities and/or intensities of the laser pulses.

For smaller ellipticities and/or intensities, the short-time expansion no longer holds, and a general theory has been provided in terms of a Kepler problem, with a rotation of the axes in the laser polarization plane. When the electron is far away from the parent-ion, the KH potential reduces to a Coulomb potential. Therefore the dynamics can be

described simply by a Kepler problem. Hence, it is relevant to see how the conserved quantities of a Kepler problem behave for the KH trajectory, especially directly after the electron's release due to the impact from the KH potential. We observed that the energy E and the angular momentum l remain approximately constant, whereas the Runge-Lenz vector (RLV) significantly changes its direction. Taking advantage of this observation, we constructed a rotated Kepler trajectory, where the change in the RLV angle provided a quantitative measure for the rotation angle. Interestingly, the constant behaviour of E and l hints at a possible static, spherical symmetric potential, which has the surprising form of a ring potential. Previous attempts have been made to formulate a time-independent description of the electron dynamics, e. g., the Rutherford scattering problem [37] and a Lie transformation method [35]. However, both theories are only valid for low-intensity pulses.

In the future, one could look for possible conserved quantities associated with the static ring potential other than E and l. This leaves room to understand the change in the RLV angle, possibly by formulating an analytical expression that would incorporate such changes.

Chapter 4 is devoted mainly to the attoclock set up with a nearly circularly-polarized pulse. Experimentally the polar angle in the photo-electron momentum plane, which is measured at the detector, is typically mapped to the electric field at the ionization time. The purpose of such a map is to gain insight into the tunnelling time. Our goal, however, was to derive an analytical expression for the attoclock offset angle, which captures the numerical results within a good agreement, not only for the single trajectory but also for the classical-trajectory Monte Carlo (CTMC) simulations with many trajectories.

The derivation of getting an analytical formula, in this context, requires the knowledge of the impulse from the KH potential. Although a perturbative expansion of the impulse up to the first-order term reproduces the exact offset angle, it does not lead to a closed-form analytical expression. Only approximations within this first-order perturbation can give an analytical solution, which holds for high and low ends of the laser intensity. In a low-intensity regime, the quiver amplitude becomes much smaller than the tunnelling exit-radius, whereas in a high-intensity regime, the reverse is satisfied. Identifying the critical intensity, which lies in the boundary of the two intensity regimes, a connection

between the two extremes is achieved, resulting in a complete analytical prediction for the offset angle as a function of intensity. The agreement of the analytically predicted angle with the classical simulation results is good for low frequency and high ellipticity. The physics behind the parameter dependence is based on two facts: the Coulomb attraction at the tunnel exit and the electron's initial momentum.

Furthermore, agreement with the experimental data has led to a new definition of the tunnel exit-radius, which has been modelled by an unconventional form, involving the physics of non-adiabatic tunnelling and depletion of the atomic ground state.

Such a formalism can also be extended to explore the attoclock with a bicircular laser pulse [103], a glimpse of which is shown in section 4.8, as a warm-up.

Appendix A

Atomic units

In this thesis, the atomic units (au) have been used regularly. Note that the following definition should be satisfied in au.

$$\hbar = m_e = e = a_0 = 1, \tag{A.1}$$

where $\hbar$ is the Planck's constant, m_e and e are respectively the mass and the charge of the electron, and a_0 is the Bohr-radius. See the corresponding SI values of these quantities from Table A.1.

Conversion factors from SI unit to au of some other useful quantities have been listed in Table A.1. For example, using this table, the following relation between wavelength λ in nm and frequency ω in au can be obtained.

$$\lambda = \frac{2\pi c}{\omega} = \frac{2\pi 137.036}{\omega}\ [\text{au}] = \frac{45.5636}{\omega\ [\text{au}]}\ [\text{nm}] \tag{A.2}$$

Quantities	SI units	Atomic units [au]
angular momentum, $\hbar$ = Planck's constant divided by 2 π	1.0546 $\times 10^{-34}$ J s	1 $\hbar$
mass, m_e	9.1094 $\times 10^{-31}$ kg	1 m_e
charge, e	1.6022 $\times 10^{-19}$ C	1 e
Bohr-radius, a_0	5.2918 $\times 10^{-11}$ m	1 a_0
permittivity in free space, $4\pi\epsilon_0$	1.1126 $\times 10^{-10}$ A s (V m)$^{-1}$	1 $m_e e^2 a_0/\hbar^2$
electron velocity in the first Bohr-orbit, $v_0 = c/137.036$	2.1877 $\times 10^{6}$ m s^{-1}	1 $\hbar/(m_e a_0)$
electron orbital-period in the first Bohr-orbit, $t_0 = a_0/v_0$	2.4189 $\times 10^{-17}$ s	1 $m_e a_0^2/\hbar$
electron angular-frequency in the first Bohr-orbit, $\nu_0 = v_0/a_0$	4.1341 $\times 10^{16}$ s^{-1}	1 $\hbar/(m_e a_0^2)$
electric field-strength felt by an electron in the first Bohr-orbit, $F_a = e/(4\pi\epsilon_0 a_0^2)$	5.1427 $\times 10^{11}$ V m^{-1}	1 $\hbar^2/(m_e e a_0^3)$
intensity corresponding to field-strength F_a, $I_a = \epsilon_0 c F_a^2/2$	3.5101 $\times 10^{16}$ W cm^{-2}	1 $\hbar^3/(m_e^2 a_0^6)$
atomic energy (calculated as twice the ionization potential) of the hydrogen atom, $2\|I_\mathrm{p}\| = e^2/(4\pi\epsilon_0 a_0)$	27.2120 eV	1 $\hbar^2/(m_e a_0^2)$

TABLE A.1: Conversion factors between SI and atomic units

Appendix B

Asymptotic momentum in a Kepler problem

For a given position and momentum $\vec{r}$, and $\vec{p}$ at any time t, the asymptotic momentum $\vec{P}$ at $t \to \infty$ can be obtained by using the two conserved quantities in a Kepler problem — the angular momentum $\vec{l}$ and the Runge-Lenz vector $\vec{a}$. Since they are constant in time, the following relations are satisfied

$$\vec{l} = \vec{r}(t) \times \vec{p}(t) = \text{constant}, \tag{B.1}$$

$$\vec{a} = \vec{p}(t) \times \vec{l} - \frac{\vec{r}(t)}{r(t)} = \text{constant}. \tag{B.2}$$

Now, we use the asymptotic property for $t \to \infty$

$$\frac{\vec{r}(t \to \infty)}{r(t \to \infty)} = \frac{\vec{P}}{P}, \tag{B.3}$$

with P being the magnitude of $\vec{P}$ as given by

$$P = \sqrt{\vec{p}(t)^2 - \frac{2}{r(t)}}. \tag{B.4}$$

The last equation is obtained from the conservation of energy. Using Eq. (B.3), the above Eq. (B.2) reduces to

$$\vec{a} = \vec{P} \times \vec{l} - \vec{P}/P. \tag{B.5}$$

From this relation, the following identity is constructed.

$$\begin{aligned} P(\vec{a}\times\vec{l})+\vec{a} &= P\Big[\Big(\vec{P}\times\vec{l}-\frac{\vec{P}}{P}\Big)\times\vec{l}\Big]+\Big(\vec{P}\times\vec{l}-\frac{\vec{P}}{P}\Big) \\ &= -\vec{P}Pl^2-\frac{\vec{P}}{P} \\ &= -\frac{\vec{P}}{P}\Big[1+P^2l^2\Big]. \end{aligned} \tag{B.6}$$

Where the cross-product properties

$$\vec{a}\times(\vec{b}\times\vec{c}) = \vec{b}(\vec{a}\cdot\vec{c})-\vec{c}(\vec{a}\cdot\vec{b}), \tag{B.7a}$$

$$(\vec{a}\times\vec{b})\times\vec{c} = \vec{b}(\vec{a}\cdot\vec{c})-\vec{a}(\vec{b}\cdot\vec{c}), \tag{B.7b}$$

and that the angular momentum lies perpendicular to the momentum, i. e.,

$$\vec{P}\cdot\vec{l}=0 \tag{B.8}$$

have been used.

Thus the general expression for the asymptotic momentum, from Eq. (B.6), reads

$$\vec{P}=P\frac{P(\vec{l}\times\vec{a})-\vec{a}}{1+P^2l^2}. \tag{B.9}$$

Appendix C

Ground state depletion (GSD)

The ground state depletion (GSD) effect in strong-field ionization is a phenomena which takes account the depletion of the atom in the presence of an intense laser. The survival probability of the atom is given by

$$\rho(t) = \exp\left(-\int_{-\infty}^{t} R_0(t')dt' \right). \tag{C.1}$$

Including this survival probability into the total ionization probability of the electron, yields Eq. (4.10). The total ionization probability cf. Eq. (4.10) is obtained, in Fig. C.1 with and without encountering GSD, for two ionization potentials $I_\mathrm{p} = 0.51$ au (Kr) and $I_\mathrm{p} = 0.9$ au (He) as a function of the initial phase $\phi_0 = \omega t_0$.

Figure C.1(a) shows that the peak of the ionization yield with GSD is shifted along the ϕ_0-axis slightly earlier than the peak of the yield without GSD. Now without the GSD effect, the yield is maximum at $\phi_0 = 0$, i. e. at the field-maximum. Including the GSD effect, when the electric field reaches its maximum, the atoms are already depleted. Therefore, the ionization slightly earlier than the field-maximum becomes more prominent than the ionization at the field-maximum. Hence, the most-probable trajectory corresponds to $F_\mathrm{max} - F_s$, not to $F_\mathrm{max} = F(\phi_0 = 0)$. Here, $F_s = F(\phi_0 = \phi_s)$ is a positive quantity with $\phi_s = \omega t_s$ being the shift in phase of the peak of the yield from the field-maximum. ϕ_s is marked by the dotted vertical-line in the figure.

The depletion effect vanishes for high I_p, as shown for He in Fig. C.1(b).

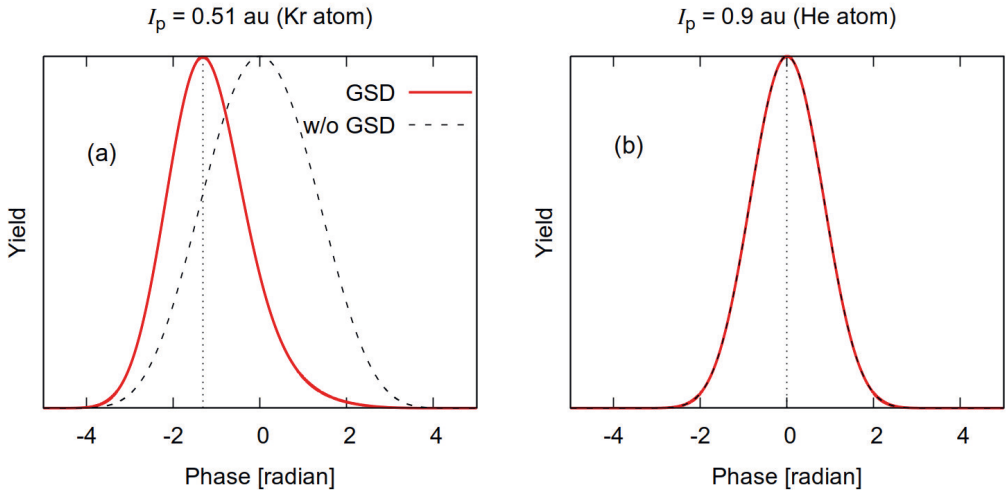

FIGURE C.1: Ionization probability with and without ground state depletion for two different ionization potential as a function of the initial phase $\phi_0 = \omega t_0$. The laser parameters used here are intensity $I = 6 \times 10^{14}$ Wcm^{-2}, wavelength $\lambda = 800$ nm for circular polarization (ellipticity $\varepsilon = 1$) with a $\cos^4$ pulse envelope containing $N = 3$ optical cycles.

Appendix D

Accelerated Kepler problem

The elliptical nuclear motion due to the presence of an elliptically-polarized laser pulse, as depicted in Fig. 3.1, can be considered by a hyperbolic motion if the relations $\cos(\omega t) = 1 - \frac{\omega^2 t^2}{2}$, and $\sin(\omega t) = \omega t$ are satisfied. Such approximations can work if the electron quickly flies off from the moving nucleus after staying for a short time near the nucleus. Therefore, we can write down the position of the nucleus with a CW pulse as

$$\vec{R}(t) = r_{\mathrm{q}}(\cos(\omega t)\vec{e}_y + \varepsilon \sin(\omega t)\vec{e}_x) \approx r_{\mathrm{q}}\left(\left(1 - \frac{\omega^2 t^2}{2}\right)\vec{e}_y + \varepsilon \omega t \vec{e}_x\right). \tag{D.1}$$

This leads to linear momentum along the y-axis, and constant momentum along the x-axis, therefore, constant acceleration along the y-axis, and zero acceleration along the x-axis. The problem becomes an accelerated Kepler problem (AKP), as discussed in [99]. We apply this method to describe the electron's motion in the KH frame, as discussed in the following.

Newton's equations of motion (eom) of an electron in the space-fixed frame with a KH potential is given by

$$\frac{d^2\vec{r}}{dt^2} = -\frac{d}{dr}\frac{-1}{|\vec{r} - \vec{r}_{\mathrm{q}}(t)|}. \tag{D.2}$$

Now, going to the relative coordinates of motion $\vec{r}_r = \vec{r} - \vec{R}$, and using $\vec{r}_{\mathrm{q}}(t) = \vec{R}(t)$ from Eq. (D.1), the above equation reduces to

$$\frac{d^2\vec{r}_r}{dt^2} = -\frac{\vec{r}_r}{|\vec{r}_r|^3} + r_{\mathrm{q}}\ \omega^2\ \vec{e}_y. \tag{D.3}$$

This is the eom of an electron in the presence of a static force. In principle, this has a closed-form solution [100]. Now, the electron's coordinate in the space-fixed frame is given by

$$\vec{r}(t) = \vec{R}(t) + \vec{r}_r(t). \tag{D.4}$$

In order to solve the above eom Eq. (D.3), we need to know the initial conditions in the relative coordinates.

The initial coordinates of the electrons as obtained from Eqs. (3.23)-(3.24), are given by

$$\vec{r}(0) = (r_e + r_{\mathrm{q}})\vec{e}_y \qquad \vec{p}(0) = r_{\mathrm{q}}\varepsilon\omega\vec{e}_x. \tag{D.5}$$

The initial coordinates of the nucleus using Eq.(D.1) are given by

$$\vec{R}(0) = r_{\mathrm{q}}\vec{e}_y \qquad \dot{\vec{R}}(0) = r_{\mathrm{q}}\varepsilon\omega\vec{e}_x. \tag{D.6}$$

This makes the initial coordinates in the relative coordinate as

$$\vec{r}_r(0) = r_e\vec{e}_y \qquad \vec{p}_r(0) = 0, \tag{D.7}$$

which makes the problem to be decoupled in x and y-direction.

Since the force in the x-direction for the eom in Eq. (D.3) is zero with zero values of initial coordinates, the motion does not change in this direction, for which the electron's coordinate in this dimension is determined entirely by the nucleus motion, which is given by

$$\vec{x}(t) = \vec{R}_x(t) = r_{\mathrm{q}}\varepsilon\omega t\vec{e}_x, \tag{D.8}$$

$$\vec{p}_x(t) = \dot{\vec{R}}_x(t) = r_{\mathrm{q}}\varepsilon\omega\vec{e}_x. \tag{D.9}$$

The motion in the y-direction is obtained by solving the eom for the following Hamiltonian corresponding to Eq. (D.3)

$$H(\vec{r}_r, \vec{p}_r) = \frac{\vec{p}_{yr}{}^2}{2} - \frac{1}{y_r} - r_{\mathrm{q}}\omega^2 y_r. \tag{D.10}$$

The final momentum $\vec{p}_{yr}(t \to \infty)$ from this equation can be obtained using a perturbation approach as has been done in [15], which gives

$$\begin{aligned}
\vec{p}_{yr}(t \to \infty) &= \vec{p}_{yr,\mathrm{l}}(t \to \infty) + \vec{p}_{yr,\mathrm{c}}(t \to \infty) \\
&= \left(0 \; - \int_0^\infty dt \frac{1}{y_r(t)^2}\right)\vec{e}_y \\
&= \left(- \int_0^\infty dt \frac{1}{[r_e + \frac{1}{2} r_\mathrm{q} \; \omega^2 \; t^2]^2}\right)\vec{e}_y \\
&= -\frac{\pi}{\sqrt{r_\mathrm{q}\omega^2 (2r_e)^3}}\vec{e}_y. \qquad \text{(D.11)}
\end{aligned}$$

Here, $\vec{p}_{yr,\mathrm{l}}(t \to \infty)$ corresponds to the final momentum in the presence of the laser only, i. e., ignoring any Coulomb interaction in the relative coordinate. This momentum is equal to $\vec{p}_{y,\mathrm{l}}(t \to \infty) - \dot{\vec{R}}_{y,\mathrm{l}}(t \to \infty)$, which reads zero since both of the terms separately are zero.

Appendix E

Different tunnel exit points

The tunnel exit-radius r_e is an important parameter in the analytical angle. Here, we analyse the intensity dependence of the analytical attoclock angle for different r_e and compare this with the corresponding CTMC simulation results. The tunnel exit point can not be traced in a real experiment, however there are various theoretical models that predict this r_e which are discussed in the following.

Considering the adiabatic tunnel ionization i. e. the ionization occurring by the instantaneous field, three models for calculating r_e are discussed in the following. The field direction model (FDM) [62]: r_e is calculated simply by using the energy conservation with zero kinetic energy at the tunnel-exit, given by

$$I_\mathrm{p} = 1/r_e + F_\varepsilon r_e, \tag{E.1}$$

The corresponding solution for the tunnel exit-radius r_e is obtained as the following

$$r_{e,\ \mathrm{FDM}} = \frac{I_\mathrm{p} + \sqrt{I_\mathrm{p}^2 - 4F_\varepsilon}}{2F_\varepsilon}. \tag{E.2}$$

In the simplest case by ignoring the Coulomb interaction term $1/r_e$ in Eq. (E.1) we obtain $r_{e,\ \mathrm{SFA}}$ as follows

$$r_{e,\ \mathrm{SFA}} = \frac{I_\mathrm{p}}{F_\varepsilon}. \tag{E.3}$$

Another model within the adiabatic tunnel ionization picture, which includes the pure Coulomb potential $1/r$, can be obtained by changing Cartesian coordinates to parabolic coordinates ([21], [98]). The interaction Hamiltonian in Eq. (2.15) but with static electric field, when written in the parabolic coordinates, can be separated into two dimensions, namely the unbound (u) and bound (v) dimensions (see the supplemental material of [53]). The electron tunnels along the u-dimension. The assumption that all the ionized-electron energy is transferred to u-dimension leads to the same exit-radius as in Cartesian-coordinate (Eq. E.2). However, in the quantum description, the energy in the v-dimension is not zero but finite and equals to the zero-point energy ($\sqrt{2I_\mathrm{p}}/2$). Therefore, from the energy conservation, there is missing energy in the u-dimension, which modifies the tunnel exit-radius as given by

$$r_{e,\ \mathrm{Para}} = \frac{I_\mathrm{p} + \sqrt{I_\mathrm{p}^2 - 4\beta F_\varepsilon}}{2F_\varepsilon}, \tag{E.4}$$

here $\beta = 1 - \sqrt{\frac{I_\mathrm{p}}{2}}$.

From Eqs. (E.2)-(E.4), it can be seen that $r_{e,\ \mathrm{FDM}} < r_{e,\ \mathrm{Para}} < r_{e,\ \mathrm{SFA}}$, with the difference becoming larger for larger intensity, as can also be observed from the inset of Fig. E.1. The attoclock offset angle θ_0, originating from the Coulomb attraction force at the tunnel-exit, falls with r_e, and follows a reverse order i. e. $\theta_{c,\ \mathrm{FDM}} > \theta_{c,\ \mathrm{Para}} > \theta_{c,\ \mathrm{SFA}}$ corresponding to the three models. This qualitative behaviour of offset angle is also sustained by our analytical angle (Eq. 4.41), as observed in Fig. E.1 (dashed curves). With the analytical angle, the offset angle θ_0 obtained from the CTMC-simulation as described in section 4.3.3 is shown for the three r_e. The figure shows that the analytical angle agrees even quantitatively with the CTMC-simulation results.

The argument within the square root of Eqs. (E.2) and (E.4) becomes zero or negative above some field amplitude F_ε, and the corresponding process is known as over barrier ionization (OBI). Because of the factor-β in $r_{e,\mathrm{Para}}$, the OBI field amplitude with $r_{e,\mathrm{Para}}$ is always larger than with $r_{e,\mathrm{FDM}}$. Whereas, with the SFA exit-radius $r_{e,\mathrm{SFA}}$, cf. Eq. (E.3), there is no such OBI process. Therefore, r_e should be chosen depending on the purpose of the problem.

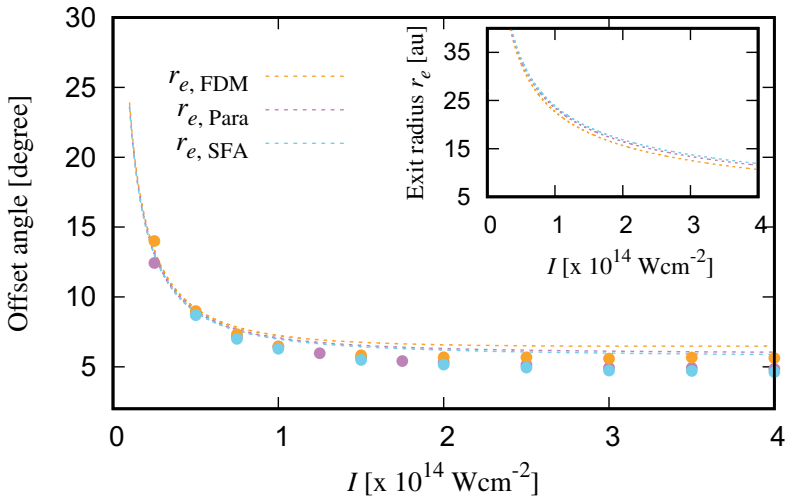

FIGURE E.1: Offset angle as a function of intensity I for three different models of tunnel exit-radius r_e shown in the inset. The dashed curves and points represent respectively the results from the analytical and CTMC-simulation calculations. Parameters are the same as in Fig. 4.4.

Bibliography

[1] *The Nobel Prize in Physics 2018, https://www.nobelprize.org/prizes/physics/2018/summary/.* .

[2] R. Pazourek, S. Nagele, and J. Burgdörfer, *Time-resolved photoemission on the attosecond scale: opportunities and challenges.* Faraday Discussions **163**, 353 (2013).

[3] J. Itatani, F. Quéré, G. L. Yudin, M. Y. Ivanov, F. Krausz, and P. B. Corkum, *Attosecond Streak Camera.* Phys. Rev. Lett. **88**, 173903 (2002).

[4] E. Constant, V. D. Taranukhin, A. Stolow, and P. B. Corkum, *Methods for the measurement of the duration of high-harmonic pulses.* Phys. Rev. A **56**, 3870 (1997).

[5] V. S. Yakovlev, B. Ferdinand, and A. Scrinzi, *Attosecond streaking measurements.* J. Mod. Opt. **52**, 395 (2005).

[6] U. Saalmann and J. M. Rost, *Proper Time Delays Measured by Optical Streaking.* Phys. Rev. Lett. **125**, 113202 (2020).

[7] P. Eckle, M. Smolarski, P. Schlup, J. Biegert, A. Staudte, M. Schöffler, H. G. Muller, R. Dörner, and U. Keller, *Attosecond angular streaking.* Nat. Phys. **4**, 565 (2008).

[8] P. Eckle, A. N. Pfeiffer, C. Cirelli, A. Staudte, R. Dörner, H. G. Muller, M. Büttiker, and U. Keller, *Attosecond ionization and tunneling delay time measurements in helium.* Science **322**, 1525 (2008).

[9] S. V. Popruzhenko, *Keldysh theory of strong field ionization: History, applications, difficulties and perspectives.* J. Phys. B **47**, 204001 (2014).

[10] L. V. Keldysh, *Ionization in the field of a strong electromagnetic wave.* J. Exptl. Theoret. Phys. (U.S.S.R.) **47**, 1945 (1964).

[11] F. H. M. Faisal, *Multiple absorption of laser photons by atoms*. J. Phys. B: Atom. Mol. Phys. **6**, L89 (1973).

[12] H. R. Reiss, *Effect of an intense electromagnetic field on a weakly bound system*. Phys. Rev. A **22**, 1786 (1980).

[13] K. Amini, J. Biegert, F. Calegari, A. Chacón, M. F. Ciappina, A. Dauphin, D. K. Efimov, C. F. d. M. Faria, K. Giergiel, and P. Gniewek, *Symphony on strong field approximation*. Rep. Prog. Phys. **82**, 116001 (2019).

[14] T. Brabec, M. Y. Ivanov, and P. B. Corkum, *Coulomb focusing in intense field atomic processes*. Phys. Rev. A **54**, R2551 (1996).

[15] S. P. Goreslavski, G. G. Paulus, S. Popruzhenko, and N. I. Shvetsov-Shilovski, *Coulomb Asymmetry in Above-Threshold Ionization*. Phys. Rev. Lett. **93**, 233002 (2004).

[16] T. Nubbemeyer, K. Gorling, A. Saenz, U. Eichmann, and W. Sandner, *Strong-Field Tunneling without Ionization*. Phys. Rev. Lett. **101**, 233001 (2008).

[17] A. Kästner, U. Saalmann, and J. M. Rost, *Energy bunching in soft recollisions revealed with long-wavelength few-cycle pulses*. J. Phys. B: At. Mol. Opt. Phys. **45**, 074011 (2012).

[18] A. S. Landsman, C. Hofmann, A. N. Pfeiffer, C. Cirelli, and U. Keller, *Unified Approach to Probing Coulomb Effects in Tunnel Ionization for Any Ellipticity of Laser Light*. Phys. Rev. Lett. **111**, 263001 (2013).

[19] Q. Z. Xia, J. F. Tao, J. Cai, L. Fu, and J. Liu, *Quantum Interference of Glory Rescattering in Strong-Field Atomic Ionization*. Phys. Rev. Lett. **121**, 143201 (2018).

[20] J. Dubois, S. Berman, C. Chandre, and T. Uzer, *Inclusion of Coulomb effects in laser-atom interactions*. Phys. Rev. A **99**, 053405 (2019).

[21] A. N. Pfeiffer, C. Cirelli, M. Smolarski, D. Dimitrovski, M. Abu-samha, L. B. Madsen, and U. Keller, *Attoclock reveals natural coordinates of the laser-induced tunnelling current flow in atoms*. Nat. Phys. **8**, 76 (2012).

[22] U. S. Sainadh, H. Xu, X. Wang, A. Atia-Tul-Noor, W. C. Wallace, N. Douguet, A. Bray, I. Ivanov, K. Bartschat, A. Kheifets, R. T. Sang, and I. V. Litvinyuk, *Attosecond angular streaking and tunnelling time in atomic hydrogen*. Nature **568**, 75 (2019).

[23] N. Camus, E. Yakaboylu, L. Fechner, M. Klaiber, M. Laux, Y. Mi, K. Z. Hatsagortsyan, T. Pfeifer, C. H. Keitel, and R. Moshammer, *Experimental evidence for quantum tunneling time*. Phys. Rev. Lett. **119**, 023201 (2017).

[24] A. S. Landsman, M. Weger, J. Maurer, R. Boge, A. Ludwig, S. Heuser, C. Cirelli, L. Gallmann, and U. Keller, *Ultrafast resolution of tunneling delay time*. Optica **1**, 343 (2014).

[25] J. M. Rost and U. Saalmann, *Attoclock and tunnelling time*. Nat. Photon. **13**, 439 (2019).

[26] C. Hofmann, A. S. Landsman, and U. Keller, *Attoclock revisited on electron tunnelling time*. J. Mod. Opt. **66**, 1052 (2019).

[27] A. S. Kheifets, *The attoclock and the tunneling time debate*. J. Phys. B **53**, 072001 (2020).

[28] U. S. Sainadh, R. T. Sang, and I. V. Litvinyu, *Attoclock and the quest for tunnelling time in strong-field physics*. J. Phys. Photonics **2**, 042002 (2020).

[29] V. V. Serov, J. Cesca, and A. S. Kheifets, *Numerical and laboratory attoclock simulations on noble-gas atoms*. Phys. Rev. A **103**, 023110 (2021).

[30] L. A. MacColl, *Note on the transmission and reflection of wavepackets by potential barriers*. Phys. Rev. **40**, 621 (1932).

[31] H. A. Kramers, *The collected papers of H.A. Kramers*. Amsterdam : North-Holland Publishing Company 272 (1956.).

[32] W. C. Henneberger, *Perturbation method for atoms in intense light beams*. Phys. Rev. Lett. **21**, 838 (1968).

[33] M. Pont, N. R. Walet, M. Gavrila, and C. W. McCurdy, *Dichotomy of the Hydrogen Atom in Superintense, High-Frequency Laser Fields*. Phy. Rev. Lett. **61**, 939 (1988).

[34] M. Pont, N. R. Walet, and M. Gavrila, *Radiative Distortion of the Hydrogen Atom in Superintense, High-Frequency Fields of Linear Polarization*. Phys. Rev. A **41**, 477 (1990).

[35] J. Dubois, S. A. Berman, C. Chandre, and T. Uzer, *Capturing Photoelectron Motion with Guiding Centers*. Phys. Rev. Lett. **121**, 113202 (2018).

[36] J. Dubois, S. A. Berman, C. Chandre, and T. Uzer, *Guiding-center motion for electrons in strong laser fields*. Phys. Rev. E **98**, 052219 (2018).

[37] A. W. Bray, S. Eckart, and A. S. Kheifets, *Keldysh-Rutherford model for the atto-clock*. Phys. Rev. Lett. **121**, 123201 (2018).

[38] R. Olson, *Classical Trajectory and Monte Carlo Techniques* (Springer Handbook of Atomic, Molecular, and Optical Physics, Springer, New York, 2006).

[39] N. I. Shvetsov-Shilovski and M. Lein, *Semiclassical two-step model for strong-field ionization*. Phys. Rev. A **94**, 013415 (2016).

[40] N. I. Shvetsov-Shilovski and M. Lein, *Semiclassical two-step model with quantum input: Quantum-classical approach to strong-field ionization*. Phys. Rev. A **100**, 053411 (2019).

[41] H. Ni, U. Saalmann, and J. M. Rost, *Tunneling exit characteristics from classical backpropagation of an ionized electron wave packet*. Phys. Rev. A **97**, 013426 (2018).

[42] H. Ni, U. Saalmann, and J. M. Rost, *Tunneling Ionization Time Resolved by Backpropagation*. Phys. Rev. Lett. **117**, 023002 (2016).

[43] A. Huillier and P. Balcou, *High-order harmonic generation in rare gases with a 1-ps 1053-nm laser*. Phys. Rev. Lett. **70**, 774 (1993).

[44] P. Agostini, F. Fabre, G. Mainfray, G. Petite, and N. K. Rahman, *Free-Free Transitions Following Six-Photon Ionization of Xenon Atoms*. Phys. Rev. Lett. **42**, 1127 (1979).

[45] B. HuP, J. Liu, and S.-g. Chen, *Plateau in above-threshold-ionization spectra and chaotic behavior in rescattering processes*. Phys. Lett. A **236**, 533 (1997).

[46] K. I. Dimitriou, D. G. Arbó, S. Yoshida, E. Persson, and J. Burgdörfe, *"Origin of the double-peak structure in the momentum distribution of ionization of hydrogen atoms driven by strong laser fields*. Phys. Rev. A **70**, 061401 (2004).

[47] C. I. Blaga, F. Catoire, P. Colosimo, G. G. Paulus, H. G. Muller, P. Agostini, and L. F. DiMauro, *Strong-field photoionization revisited*. Nat. Phys. **5**, 335 (2009).

[48] C. Liu and K. Z. Hatsagortsyan, *Origin of unexpected low energy structure in photoelectron spectra induced by midinfrared strong laser fields*. Phys. Rev. Lett. **105**, 113003 (2010).

[49] A. Kästner, U. Saalmann, and J. M. Rost, *Electron-Energy Bunching in Laser-Driven Soft Recollisions*. Phys. Rev. Lett. **108**, 033201 (2012).

[50] C. Lemell, K. I. Dimitriou, X.-M. Tong, S. Nagele, D. V. Kartashov, J. Burgdörfer, and S. Gräfe, *Low-energy peak structure in strong-field ionization by midinfrared laser pulses: Two-dimensional focusing by the atomic potential*. Phys. Rev. A **85**, 011403 (2012).

[51] J. Dura, N. Camus, A. Thai, A. Britz, M. Hemmer, M. Baudisch, A. Senftleben, C. D. Schroter, J. Ullrich, R. Moshammer, and J. Biegert, *Ionization with low-frequency fields in the tunneling regime*. Sci. Rep. **3**, 2675 (2013).

[52] M. G. Pullen, J. Dura, B. Wolter, M. Baudisch, M. Hemmer, N. Camus, A. Senftleben, C. D. Schroeter, R. Moshammer, and J. Ullrich, *Kinematically complete measurements of strong field ionization with mid-IR pulses*. J. Phys. B: At. Mol. Opt. Phys. **47**, 204010 (2014).

[53] E. Diesen, U. Saalmann, M. Richter, M. Kunitski, R. Dörner, and J. M. Rost, *Dynamical Characteristics of Rydberg Electrons Released by a Weak Electric Field*. Phy. Rev. Lett. **116**, 143006 (2016).

[54] O. Svelto, *Principles of Lasers* (Plenum Press, New York, 1998).

[55] T. W. Hänsch, *A proposed sub-femtosecond pulse synthesizer using separate phase-locked laser oscillators*. Opt. Commun. **80**, 71 (1990).

[56] P. Antoine, A. L'Huillier, and M. Lewenstein, *Attosecond Pulse Trains Using High–Order Harmonics*. Phys. Rev. Lett. **77**, 1234 (1996).

[57] P. M. Paul, E. S. Toma, P. Breger, G. Mullot, F. Augé, P. Balcou, H. G. Muller, and P. Agostini, *Observation of a Train of Attosecond Pulses from High Harmonic Generation*. Science **292**, 1689 (2001).

[58] H. R. Reiss, *Focus Issue: Relativistic Effects in Strong Fields*. Opt. Exp. **2**, 261 (1998).

[59] H. R. Reiss, *Dipole-approximation magnetic fields in strong laser beams*. Phys. Rev. A **63**, 013409 (2000).

[60] J. D. Jackson, *Classical Electrodynamics* (Wiley, New York, 1999).

[61] F. Grossmann, *Theoretical Femtosecond Physics* (Springer Series, Springer-Verlag Berlin Heidelberg, 2008).

[62] M. Y. Ivanov, M. Spanner, and O. Smirnova, *Anatomy of strong field ionization*. J. Mod. Opt. **52**, 165 (2005).

[63] G. Mainfray and C. Manus, *Multiphoton ionization of atoms*. Rep. Prog. Phys. **54**, 1333 (1991).

[64] R. Kienberger, E. Goulielmakis, M. Uiberacker, A. Baltuska, V. Yakovlev, F. Bammer, A. Scrinzi, T. Westerwalbesloh, U. Kleineberg, U. Heinzmann, M. Drescher, and F. Krausz, *Atomic transient recorder*. Nature **427**, 817 (2004).

[65] I. Y. Kiyan and V. P. Krainov, *Above-barrier ionization of the hydrogen atom in a superstrong optical field*. Zh. Eksp. Teor. Fiz. **100**, 776 (1991).

[66] L. D. Landau and E. M. Lifshitz, *Course Of Theoretical Physics*. Quantum mechanics **3**, Third edition (1989).

[67] M. V. Ammosov, N. B. Delone, and V. P. Krainov, *Tunnel ionization of complex atoms and atomic ions in a varying electromagnetic-field*. Zh. Eksp. Teor. Fiz. **91**, 2008 (1986).

[68] N. B. Delone and V. P. Krainov, *Energy and angular electron spectra for the tunnel ionization of atoms by strong low-frequency radiation*. J. Opt. Soc. Am. B **8**, 6 (1991).

[69] X. M. Tong, Z. X. Zhao, and C. D. Lin, *Theory of molecular tunneling ionization*. Phys. Rev. A **66**, 033402 (2002).

[70] G. L. Yudin and M. Y. Ivanov, *Nonadiabatic tunnel ionization: Looking inside a laser cycle*. Phys. Rev. A **64**, 013409 (2001).

[71] V. D. Mur, S. V. Popruzhenko, and V. S. Popov, *Energy and momentum spectra of photoelectrons under conditions of ionization by strong laser radiation (The case of elliptic polarization)*. J. Exptl. Theoret. Phys. (U.S.S.R) **92**, 777 (2001).

[72] A. M. Perelomov, V. S. Popov, and M. V. Terent'ev, *Ionization of atoms in an alternating electric field*. J. Exptl. Theoret. Phys. (U.S.S.R) **50**, 1393 (1966).

[73] V. S. Popov, *Tunnel and multiphoton ionization of atoms and ions in a strong laser field (Keldysh theory)*. Phys.-Usp. **47**, 855 (2004).

[74] P. Corkum, *Plasma Perspective on Strong-Field Multiphoton Ionization*. Phys. Rev. Lett. **71**, 1994 (1993).

[75] K. C. Kulander, K. J. Schafer, and J. L. Krause, *Super-Intense Laser-Atom Physics*. New York:Plenum Press, p.95 (1993).

[76] F. Krausz and M. Ivanov, *Attosecond physics*. Rev. Mod. Phys. **81**, 163 (2009).

[77] G. G. Paulus, W. Becker, W. Nicklich, and H. Walther, *Rescattering effects in above-threshold ionization: a classical model*. J. Phys. B: At. Mol. Opt. Phys. **27**, L703 (1994).

[78] Z. Chang, *Fundamentals of Attosecond Optics*. CRC Press. p. 84. (2016).

[79] A. S. Landsman and U. Keller, *Tunnelling time in strong field ionisation*. J. Phys. B: At. Mol. Opt. Phys. **47**, 204024 (2014).

[80] T. Zimmermann, S. Mishra, B. R. Doran, D. F. Gordon, and A. S. Landsman, *Tunneling Time and Weak Measurement in Strong Field Ionization*. Phys. Rev. Lett. **116**, 233603 (2016).

[81] L. Torlina, F. Morales, J. Kaushal, I. Ivanov, A. Kheifets, A. Zielinski, A. Scrinzi, H. G. Muller, S. Sukiasyan, M. Ivanov, and O. Smirnova, *Interpreting attoclock measurements of tunnelling times*. Nat. Phys. **11**, 503 (2015).

[82] N. I. Shvetsov-Shilovski and M. Lein, *Effects of the Coulomb potential in interference patterns of strong-field holography with photoelectrons*. Phys. Rev. A **97**, 013411 (2018).

[83] J. Liu, Y. Fu, W. Chen, Z. Lü, J. Zhao, J. Yuan, and Z. Zhao, *Offset angles of photocurrents generated in few-cycle circularly polarized laser fields*. J. Phys. B **50**, 055602 (2017).

[84] R. Boge, C. Cirelli, A. S. Landsman, S. Heuser, A. Ludwig, J. Maurer, M. Weger, L. Gallmann, and U. Keller, *Probing Nonadiabatic Effects in Strong-Field Tunnel Ionization*. Phys. Rev. Lett. **111**, 103003 (2013).

[85] D. Shafir, H. Soifer, C. Vozzi, A. S. Johnson, A. Hartung, Z. Dube, D. M. Villeneuve, P. B. Corkum, N. Dudovich, and A. Staudte, *Trajectory-Resolved Coulomb Focusing in Tunnel Ionization of Atoms with Intense, Elliptically Polarized Laser Pulses*. Phys. Rev. Lett. **111**, 023005 (2013).

[86] G. L. Yudin and M. Y. Ivanov, *Physics of correlated double ionization of atoms in intense laser fields: Quasistatic tunneling limit*. Phys. Rev. A **63**, 033404 (2001).

[87] L. Medisauskas, U. Saalmann, and J. M. Rost, *Floquet Hamiltonian approach for dynamics in short and intense laser pulses*. J. Phys. B: At. Mol. Opt. Phys. **52**, 015602 (2019).

[88] O. Ciftja, A. Babineaux, and N. Hafeez, *The electrostatic potential of a uniformly charged ring*. Eur. J. Phys. **30**, 623 (2009).

[89] D. Kleppner and R. Kolenkow, *An Introduction to Mechanics*. Tata McGraw-Hill 9th reprint, (2010).

[90] S. V. Popruzhenko and T. A. Lomonosova, *Frustrated ionization of atoms in the multiphoton regime*. Laser Phys. Lett. **18**, 015301 (2021).

[91] R. Dörner, V. Mergel, O. Jagutzki, L. Spielberger, J. Ullrich, R. Moshammer, and H. Schmidt-Böcking, *Cold target recoil ion momentum spectroscopy: A 'momentum microscope' to view atomic collision dynamics*. Phys. Rep. **330**, 95 (2000).

[92] L. MacColl, *Note on the Transmission and Reflection of Wave Packets by Potential Barriers*. Phys. Rev. **40**, 621 (1932).

[93] R. Landauer, *Barrier traversal time*. Nature **341**, 567 (1989).

[94] A. N. Pfeiffer, C. Cirelli, M. Smolarski, and U. Keller, *Recent attoclock measurements of strong field ionization*. Chem. Phys. **414**, 84 (2013).

[95] N. I. Shvetsov-Shilovski, D. Dimitrovski, and L. B. Madsen, *Ehrenfest's theorem and the validity of the two-step model for strong-field ionization*. Phys. Rev. A **87**, 013427 (2013).

[96] W. H. Press, S. A. Teukolsky, W. T. Vetterling, and B. P. Flannery, *Numerical Recipes 3rd edn*. New York: Cambridge University Press (2007).

[97] R. Xu, T. Li, and X. Wang, *Longitudinal momentum of the electron at the tunneling exit*. Phys. Rev. A **98**, 053435 (2018).

[98] A. S. Landsman and U. Keller, *Attosecond science and the tunnelling time problem*. Phys. Rep. **547**, 1 (2015).

[99] F. Namouni and M. Guzzo, *The accelerated Kepler problem*. Celest. Mech. Dyn. Astr. **99**, 31 (2007).

[100] G. Lantoine and R. P. Russell, *Complete closed-form solutions of the Stark problem*. Celest. Mech. Dyn. Astr. **109**, 333 (2011).

[101] N. I. Shvetsov-Shilovski, S. P. Goreslavski, S. Popruzhenko, and W. Becker, *Capture into rydberg states and momentum distributions of ionized electrons*. Laser Phys. **19**, 1550 (2009).

[102] H. Goldstein, *Classical Mechanics*. Addison-Wesley (1951).

[103] N. Eicke and M. Lein, *Attoclock with counter-rotating bicircular laser fields*. Phys. Rev. A **99**, 031402(R) (2019).

Acknowledgements

My first and foremost acknowledgment to Prof. Jan Michael Rost and Prof. Ulf Saalmann for mentoring me throughout my PhD works. They have introduced and guided me in the field of strong-field physics. I am very much thankful to them for their scientific and sincere support during my PhD journey.

I sincerely acknowledge the Max Planck Institute for the Physics of Complex Systems (MPI-PKS) and International Max Planck Research School (IMPRS) for funding my doctoral programme, and providing me the opportunity to present my works through talks and posters.

I am thankful to Cornelia Hofmann, Fermín Rodríguez Hernández, David Walther Schönleber, Andreas Rubisch for their help during the initial period of my stay in Dresden. I am grateful to Sebastian Gemsheim for organizing the strong-field physics discussion group from where I got to learn many things.

I am also thankful to the department of visitor's programme, IT, reception, and library at MPI-PKS for all their help during my stay in these four years.

I sincerely acknowledge the unconditional support from my family members particularly my father Soumen Kumar Dutta, my mother Tapasi Datta, and my dearest friend Sayak Ray. I am also thankful to my friends, group members, and the MPI-PKS community for their support throughout my PhD works.

Declaration/Versicherung

Ich erkläre dass die in dieser Arbeit vorgestellten Forschungsarbeiten und verwandten Inhalte zur Erlangung des Doktors rerum naturalium (Dr. rer. Nat.) Das Ergebnis meinerpersönlichen Bemühungen unter Anleitung meines Betreuers, Prof. Dr. Jan-Michael Rost und Prof. Dr. Ulf Saalmann. Alle meine Arbeiten wurden am Max Planck Institut für Physik komplexer Systeme in Dresden durchgeführt.

In Anlehnung an die Ethik und Maximen der wissenschaftlichen Berichterstattung und Dokumentation wurden gebührende Anerkennungen und Zitate gemacht, wo immer derInhalt der Arbeit auf zuvor gemeldeten Arbeiten basiert oder sich auf diese bezieht. Jegliche Auslassung, die aufgrund von Versehen aufgetreten sein könnte, ist unbeabsichtigt und wird bedauert.

16.04.2021

Datum

Unterschrift